REVIEW

Check for updates

Journal of
Sensor Science and Technology

The Korean Sensors Society

Sniffing Disease: Chemiresistive Metal-Oxide Electronic Noses for Noninvasive Disease Diagnosis

Jung-Won An[1,2], Ho Won Jang[2,3], and Ji-Soo Jang[1,+]

[1]*Electronic and Hybrid Materials Research Center, Korea Institute of Science and Technology, 5 Hwarang-ro 14-gil, Seongbuk-gu, Seoul, 02791, Republic of Korea*
[2]*Department of Materials Science and Engineering, Research Institute of Advanced Materials, Seoul National University, 1 Gwanak-ro, Gwanak-gu, Seoul, 08826, Republic of Korea*
[3]*Advanced Institute of Convergence Technology, Seoul National University, Gwanggyo-ro 145, Yeongtong-gu, Suwon, 16229, Republic of Korea*

Cite This: *J. Sens. Sci. Technol. Vol. 34, No. 6 (2025) 729-749*

https://doi.org/10.46670/JSST.2025.34.6.729

ABSTRACT: This review examines recent advances in chemiresistive metal-oxide semiconductor (MOS) gas sensors for noninvasive disease diagnosis through the detection of volatile organic compounds (VOCs) in exhaled breath and skin gas. The operating principle, based on oxygen chemisorption and desorption, is first outlined along with strategies for enhancing sensor performance, including nanostructuring, catalytic functionalization, and heterojunction engineering, which enable detection limits suitable for clinical analysis (sub-ppb range). To address limitations in sensitivity and selectivity, the integration of cross-reactive sensor arrays (electronic noses) with artificial intelligence–based pattern recognition, particularly deep neural networks (DNNs), is highlighted as a critical approach for classifying complex VOC signatures. Clinical case studies across major diseases—such as lung cancer (aromatic and alkane markers), diabetes (acetone), asthma (H_2S), COVID-19 (multi-array DNN systems), and tuberculosis (multiple VOCs)—demonstrate high diagnostic accuracy, validating the technology's potential as a rapid and low-cost screening tool. However, successful clinical implementation requires overcoming key challenges, including the standardization of sampling and pre-treatment methods (e.g., end-tidal breath collection and humidity control), cross-site data generalization, mitigation of confounding variables, and improvement of long-term sensor stability. Future research should focus on advanced material systems and robust machine learning frameworks to realize universally applicable point-of-care diagnostic platforms.

KEYWORDS: *Gas sensors, Oxide semiconductors, Noninvasive diagnosis, Biomarker gas, VOCs*

1. INTRODUCTION

In healthcare, the demand for noninvasive and rapid disease screening and diagnosis has grown substantially in recent years [1,2]. Conventional diagnostic methods—such as imaging, tissue biopsy, and blood or urine analysis—offer high accuracy but are often limited by invasiveness, long processing times, high costs, and dependence on skilled personnel [2,3]. Consequently, gas-sensing technologies that utilize volatile organic compounds (VOCs) naturally emitted from the human body have emerged as promising alternatives for detecting metabolic and inflammatory signals associated with disease states [4,5].

During the onset and progression of diseases, structural and metabolic alterations in cells lead to systematic changes in the composition and concentration patterns of VOCs, as demonstrated in numerous studies [6-9]. Exhaled breath contains hundreds of VOC species—such as acetone, methanol, ethanol, and isoprene—whose compositional shifts are correlated with various respiratory and metabolic disorders [10-12]. Similarly, both endogenous and exogenous VOCs are emitted from the skin, and pattern differences can indicate the presence or absence of diseases [2,7,9].

Several studies have identified specific VOC biomarkers in exhaled breath and skin associated with particular diseases. For instance, the breath acetone concentration in diabetic patients typically exceeds 1.8 ppm, two to six times higher than that in healthy individuals (0.3–0.9 ppm), reflecting excessive ketone production due to impaired glucose regulation [13,14]. In lung cancer, distinctive variations in the

+Corresponding author: wkdwltn92@kist.re.kr
Received : Sep. 26, 2025, Revised : Oct. 11, 2025, Accepted : Oct. 19, 2025

composition and concentration of alkanes, benzenes, and toluene have been observed compared to those in healthy subjects [6,10-12,15]. In asthma, subtle changes in H_2S concentrations associated with airway inflammation suggest the potential for monitoring disease activity through exhaled breath biomarkers [16]. Likewise, in tuberculosis, variations in candidate VOCs such as toluene and acetic acid have been detected not only in exhaled breath but also in skin gas, suggesting a novel, non–sputum-based screening pathway [17].

To achieve reliable clinical discrimination using these biomarkers, ultralow concentration (ppb-level) detection is essential [3,18]. Although conventional analytical techniques such as gas chromatography–mass spectrometry (GC–MS) provide excellent accuracy, their bulkiness, high cost, and dependence on trained operators hinder their application in large-scale screening or continuous monitoring [1]. To overcome these challenges, compact, low-cost, and easily fabricated chemiresistive gas sensors have emerged as powerful candidates for medical diagnostics [4,5]. In particular, metal-oxide semiconductor (MOS) sensors operate through reactions between adsorbed oxygen species and target gases. Their response sensitivity and selectivity can be significantly enhanced through nanostructuring and catalytic functionalization with noble metals such as Pt, Pd, and Au [1,4]. Moreover, assembling sensors with diverse active layers into cross-reactive arrays and integrating them with artificial intelligence (AI)–based pattern recognition systems—forming so-called electronic noses—enables rapid and reliable classification of complex VOC "breath-print" patterns without requiring molecular identification [3,5].

Indeed, classification performances of approximately 95% have been reported in COVID-19 diagnostic trials using MOS arrays with deep neural network (DNN) analysis [19,20], while similar approaches for tuberculosis have met the World Health Organization (WHO) criteria for non–sputum-based screening [21,22].

This review summarizes the fundamental operating principles of chemiresistive gas sensors, compares sensor designs and AI-driven classification results across major disease diagnostics (lung cancer, diabetes, asthma, COVID-19, and tuberculosis), and discusses key challenges and future directions for their clinical implementation.

2. CHEMIRESISTIVE GAS SENSORS

Gas sensors can be broadly classified into several types: mass-sensitive sensors (e.g., surface acoustic wave resonators, micro/nano cantilevers, quartz crystal microbalances) [23-31]; chemiresistive sensors (e.g., metal-oxide semiconductors, polymers, two-dimensional materials, carbon-based nanostructures) [32-37]; colorimetric sensors (e.g., printable pastes, dye-functionalized textiles) [38-40]; and optical sensors (e.g., micro-/nano-LEDs, plasmonic lasers, femtosecond lasers) [41-47]. Among these, metal-oxide semiconductor (MOS)-based chemiresistive sensors are the most widely utilized for detecting VOCs due to their advantages of low cost, rapid response, simple signal readout, durability, and long operational lifetime [48].

However, their selectivity remains limited, a drawback that can be mitigated through the use of physical or chemical filter layers or by combining multiple sensor layers and processing their outputs with artificial intelligence (AI).

MOS sensor arrays integrated into electronic-nose (e-nose) systems have been extensively employed in fields such as environmental monitoring and medical diagnostics [32,36].

2.1 Operating Principles of Chemiresistive Gas Sensors

Chemiresistive gas sensors function by detecting changes in electrical resistance resulting from charge-transfer processes during the adsorption and desorption of gas molecules on the surface of a metal-oxide semiconductor. Metal-oxide nanostructures typically possess high specific surface areas and porous morphologies that facilitate strong interactions with gas molecules, making them well suited for detecting various disease-related volatile organic compounds (VOCs). Among chemiresistive gas sensors, metal-oxide semiconductors (MOSs) are the most representative and are categorized as *n-type* or *p-type* based on the dominant charge carriers [4,49].

For *n-type* semiconductors, such as SnO_2 and WO_3, oxygen molecules in ambient air are chemisorbed onto the sensor surface at elevated temperatures (typically 200–400°C), forming adsorbed oxygen species (O_2^-, O^-, O_2^{2-}). During this process, electrons from the conduction band are captured by the oxygen species, generating a surface depletion layer and increasing the sensor resistance to a steady-state value, known as the baseline resistance in air (R_{air}) (Fig. 1(a)). When a reducing gas is introduced, it reacts with the chemisorbed oxygen species, releasing trapped electrons back into the conduction band. Consequently, the depletion layer becomes thinner, and the sensor resistance decreases to a new value (R_{gas}) corresponding to the gas-exposure condition (Fig. 1(b)). Upon re-exposure to air, oxygen molecules are readsorbed, restoring both the depletion layer and the resistance to their original states (Fig. 1(c)).

Conversely, *p-type* oxides such as NiO and Co_3O_4 form a hole accumulation layer when oxygen anions are adsorbed on their surfaces, facilitating current flow and resulting in relatively low resistance (Fig. 1(d)).

When a reducing gas is introduced, electrons recombine with holes, decreasing the hole concentration and thinning the

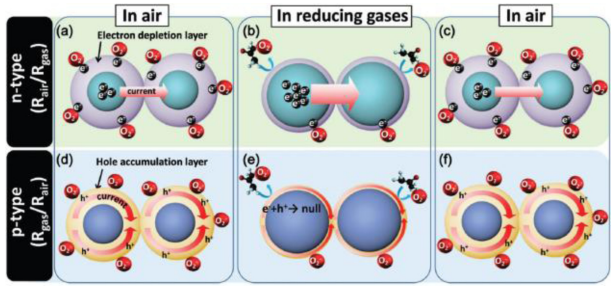

Fig. 1. Schematic illustration of gas-sensing mechanisms. (a–c) n-type MOS sensing layer; (d–f) p-type MOS sensing layer. Adapted from Ref. [4].

accumulation layer, which increases the overall resistance (Fig. 1(e)). Upon re-exposure to air, oxygen adsorption is restored, and the resistance decreases to its baseline level (Fig. 1(f)). Thus, the ratio or relative change between the baseline resistance in air (R_{air}) and the resistance under target gas exposure (R_{gas}) defines the sensor 'response,' a key metric for distinguishing various reducing and oxidizing gases [4,49].

2.2 Performance Enhancement Strategies and Pattern Recognition

Advanced nanomaterial engineering strategies are essential to maximize the sensitivity and selectivity of chemiresistive semiconductor gas sensors [4]. The chemical response of these sensors can be significantly improved through surface structural control and functionalization with catalytically active materials. First, nanostructuring, which involves the formation of complex MOS architectures such as nanofibers, nanorods, and nanospheres, enhances the specific surface area and shortens gas-molecule diffusion paths [3,50-52]. These designs improve analyte accessibility to the active layer, enabling strong responses even at low analyte concentrations [1,4]. Second, catalytic functionalization further enhances surface reactivity by decorating the MOS surface with noble metal nanoparticles (e.g., Pt, Pd, Au). These catalytic sites promote the decomposition and oxidation of target VOCs, lower activation barriers for surface reactions, and substantially improve both sensitivity and selectivity toward specific gases [1,52]. Finally, heterojunction and doping strategies, achieved by forming p–n heterojunctions, n–n or p–p homojunctions, or introducing selective dopants, enable precise control of interfacial depletion layers and barrier properties. These approaches enhance responsivity and enable ultrasensitive gas detection [18,53-55].

To overcome the limited selectivity of individual sensors and classify complex VOC mixtures, cross-reactive sensor arrays (commonly known as electronic noses (e-noses)) comprising multiple sensing elements with distinct active layers have been developed [4]. An e-nose constructs a feature vector from the outputs of its sensor array, which may include static and dynamic features, maximum amplitudes, response and recovery times, and statistical descriptors. These data are then processed using AI-based pattern recognition algorithms to determine disease states [56-61]. Both unsupervised methods, such as principal component analysis (PCA) and k-means clustering, and supervised learning algorithms, including linear discriminant analysis (LDA), support vector machines (SVM), multilayer perceptrons (MLP), and deep neural networks (DNNs), have been used to analyze composite VOC signatures and optimize classification performance. Hardware and operational strategies are crucial for addressing clinical environmental variables. The high humidity of exhaled breath interferes with the equilibrium of adsorbed oxygen species on MOS surfaces, while the competitive adsorption of water molecules on conduction pathways and active sites leads to baseline drift, reduced response, and long-term instability. To mitigate humidity effects, material-level strategies have included moisture-barrier or moisture-absorbing coatings, pore-structure control, selection of moisture-stable metal oxides, and incorporation of heterojunction materials [62-68]. System-level approaches have utilized HEPA filtration, desiccant modules, and embedded temperature and humidity sensors for real-time compensation [69,70]. On the software side, baseline normalization, humidity-aware compensation, temperature-cycling–based feature extraction, multi-sensor data fusion, and machine-learning–based correction models have been developed to suppress or disentangle humidity-induced artifacts [71,72]. Integrating these complementary approaches enhances reproducibility and facilitates field deployment in clinical environments.

Additionally, operational protocols that regulate purge–sampling–recovery cycles and maintain baseline calibration under ambient air conditions are essential for ensuring signal reproducibility and long-term stability [18]. Ultimately, through integration with the Internet of Things (IoT) paradigm, chemiresistive gas sensors are evolving into smart sensing platforms capable of real-time monitoring and intelligent automation [73].

3. DISEASE-SPECIFIC DIAGNOSTIC CASE STUDIES

3.1 Exhaled-Breath-Based Diagnosis

Exhaled breath contains hundreds of volatile organic compounds (VOCs) that reflect the body's pathophysiological and metabolic states [16], providing an effective, noninvasive, and rapid route for disease screening.

Numerous studies have demonstrated correlations between breath VOC profiles and various respiratory and metabolic diseases, including esophageal and gastric cancers, lung cancer, asthma, and tuberculosis [74,75]. High-resolution analytical techniques—such as gas chromatography–mass spectrometry (GC–MS) [9,18], ion flow tube mass spectrometry (IFT–MS) [76], laser absorption spectroscopy [77], infrared spectroscopy [78], polymer-coated surface acoustic wave (SAW) sensors [11], and coated quartz crystal microbalance (QCM) sensors [79]—have been employed to quantitatively and qualitatively assess major VOC constituents (e.g., acetone, methanol, ethanol, propanol, and isoprene) and their compositional variations.

Although these analytical techniques offer high accuracy and enable biomarker identification, they are typically bulky, complex, expensive, and relatively slow. In addition, achieving sufficient response sensitivity often requires preconcentration steps to increase VOC concentrations to detectable levels. Such preprocessing procedures, combined with the need for trained personnel and long analysis times, limit the applicability of these systems for large-scale field screening. To overcome these limitations, electronic-nose (e-nose) systems have been extensively developed and adopted. Even without identifying individual molecular species, e-noses can rapidly classify breath samples based on their characteristic response patterns. This approach enhances patient convenience and safety while offering high speed, low cost, and excellent portability [80,81].

However, exhaled-breath composition can be influenced by several external and physiological factors, including breathing patterns, diet, alcohol consumption, smoking habits, comorbidities, and environmental VOC exposure. Therefore, the standardization of sampling protocols, such as collecting the third exhalation to obtain end-tidal breath, and incorporating humidity and temperature compensation, as well as background air management, are essential. Implementing these standardized procedures minimizes confounding biases and improves measurement reproducibility.

It is also important to note that the required response sensitivity varies by disease. For instance, in diabetes, breath acetone concentrations typically exceed 1.8 ppm—compared with 0.3–0.9 ppm in healthy individuals—making sub-ppm detection clinically relevant. In lung cancer, toluene concentrations of several tens of ppb (approximately 30 ppb) have been reported as diagnostically significant. These sensitivity requirements can be met through the chemiresistive sensor design strategies discussed in subsequent sections, including nanostructuring, catalytic functionalization, and array-based pattern recognition.

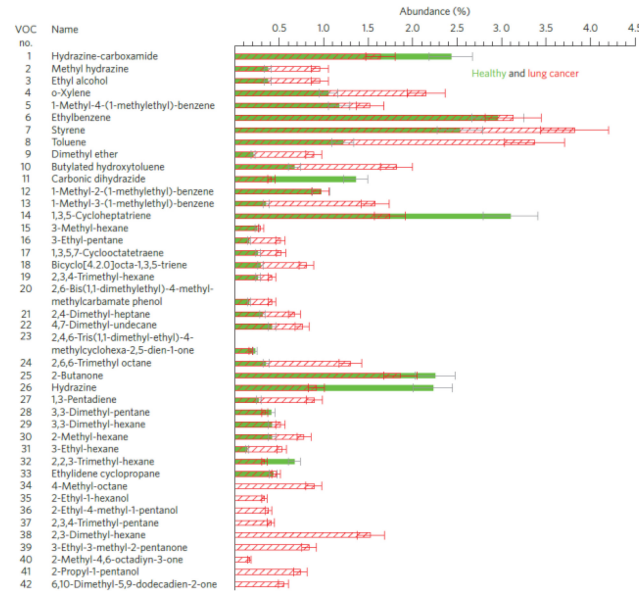

Fig. 2. Gas chromatography–mass spectrometry (GC–MS) analysis of exhaled breath from healthy individuals and lung cancer patients. Adapted from Ref. [3].

3.1.1 Lung Cancer Diagnosis

Lung cancer remains the leading cause of cancer-related deaths worldwide, accounting for approximately 13 million fatalities annually and representing nearly 28% of all cancer deaths [6,82]. Early diagnosis remains challenging, and conventional methods such as imaging and biopsy are inherently invasive. Consequently, noninvasive diagnostic approaches that utilize VOCs present in exhaled breath have gained increasing attention as promising alternatives [10-12].

In this context, Professor Hossam Haick and his research group at the Technion – Israel Institute of Technology were among the first to develop a noninvasive device capable of distinguishing lung cancer patients from healthy individuals. Initially, the group employed solid-phase microextraction (SPME) combined with gas chromatography–mass spectrometry (GC–MS) to differentiate VOC profiles in the exhaled breath of 40 cancer patients and 56 healthy controls. The analysis identified approximately 300–400 distinct VOCs, and repeated measurements over six months demonstrated a reproducibility exceeding 87%. According to the GC–MS results, 33 VOC species exhibited higher concentrations in the breath of cancer patients than in that of healthy individuals, as illustrated by the average occurrence ratios shown in Fig. 2.

Subsequently, the researchers designed an array composed of nine chemiresistive sensors (Fig. 3(a)). Each sensor was functionalized with 5 nm gold nanoparticles modified with different organic ligands, providing differential chemical reactivity toward diverse VOCs. As illustrated in Fig. 3(b),

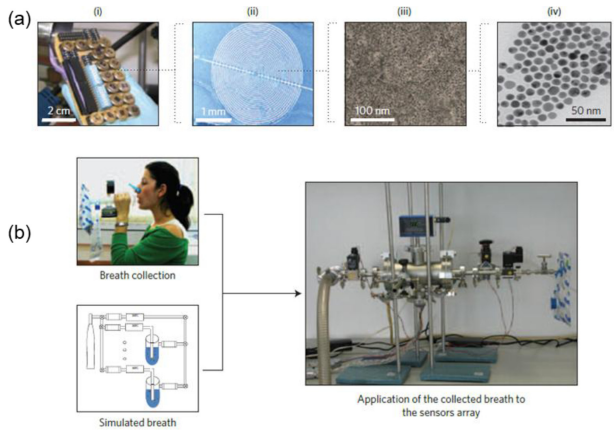

Fig. 3. Illustration of lung cancer diagnosis using breath testing. (a) (i) Photograph of the chemiresistor array, (ii) scanning electron microscopy (SEM) image of a chemiresistor, (iii) SEM image of a gold nanoparticle film located between two electrodes, and (iv) transmission electron microscopy (TEM) image of monolayer-capped gold particles. (b) Testing of exhaled breath (collected from patients) and simulated breath (a mixture of representative VOCs at concentrations similar to those determined by GC–MS analysis of exhaled patient breath) using the gold nanoparticle sensor array. Adapted from Ref. [3].

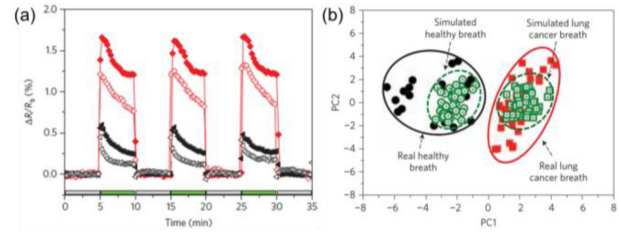

Fig. 4. Response and analysis of chemiresistors to real breath samples. (a) Response, $\Delta R/R_b$ (where R_b is the baseline resistance of the sensor in the absence of analyte and ΔR is the baseline-corrected steady-state resistance change upon exposure of the sensor to analyte) of 11-mercapto-1-undecanol–gold nanoparticles (red circles) and decanethiol–gold nanoparticles (black squares) upon exposure to healthy breath (filled symbols) and lung cancer breath (open symbols), as representative examples for sensors having positive responses. The sensors show a decrease in resistance, most likely due to increase in the permittivity of the organic matrix surrounding the metal cores. (b) Principal component analysis (PCA) of the dataset comprising real and simulated breath samples. Adapted from Ref. [3].

exhaled breath samples collected from both healthy individuals and cancer patients were exposed to the sensor array for response measurements. The fabricated sensors were tested using real clinical breath samples. As shown in Fig. 4(a), the sensor responses were consistent with the GC–MS analysis, exhibiting stronger signals for breath samples from patients with cancer than from healthy participants. In the figure, filled symbols represent healthy participants, whereas open symbols denote patients with cancer.

Beyond individual sensor responses, the combined data from all nine sensors were processed using principal component analysis (PCA) to evaluate the discrimination performance between the two groups.

As shown in Fig. 4(b), the breath patterns of cancer patients and healthy individuals were clearly separated without overlap, demonstrating excellent classification capability. The simulated breath-pattern region (highlighted in green) closely matched the actual measurement results, confirming that the array was appropriately trained for classification. Furthermore, the system achieved over 86% classification accuracy and greater than 90% reproducibility across multiple measurement days, indicating robust and consistent performance. Notably, high discrimination accuracy was achieved without any preprocessing of exhaled breath samples, demonstrating the feasibility of direct clinical application. The results also showed that system performance was independent of individual factors such as sex, age, and smoking status, underscoring its robustness.

This study established a foundation for large-scale investigations considering both exogenous factors (e.g., diet and alcohol intake) and endogenous variables (e.g., metabolic state and genetic background).

The close agreement between the e-nose results and the high-resolution GC–MS analysis validated the accuracy of this approach, highlighting the potential of gas-sensing technology as a low-cost, portable, and rapid screening tool for early lung cancer detection.

3.1.2 Diabetes Diagnosis

Diabetes affects more than 400 million people worldwide and is characterized by a metabolic disorder in which impaired glucose regulation enhances fatty acid metabolism. This process generates ketone bodies that are released as acetone through exhaled breath. Prolonged failure to control blood glucose levels can lead to severe complications, including cardiovascular disease, renal failure, retinopathy, and neuropathy, imposing substantial social and economic burdens. Because diabetes often lacks distinct early symptoms and is essentially irreversible, continuous management of blood glucose levels and lifestyle habits is required. Therefore, the development of early diagnostic methods for proactive detection and intervention is of paramount importance.

To achieve early and reliable diagnosis, various approaches have been explored, among which breath-acetone-based detection has recently attracted significant attention [83]. The concentration of acetone in exhaled breath varies in response to metabolic abnormalities associated with impaired glucose

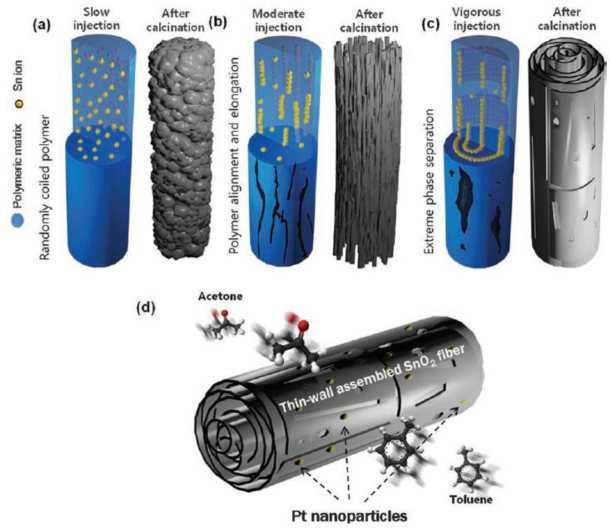

Fig. 5. Schematic illustration of the morphological evolution of as-spun and calcined SnO_2 fibers prepared at different flow rates: (a) 5 μL min^{-1}, (b) 15 μL min^{-1}, (c) 25 μL min^{-1}, and (d) Pt-decorated thin-wall assembled SnO_2 fibers. Adapted from Ref. [1].

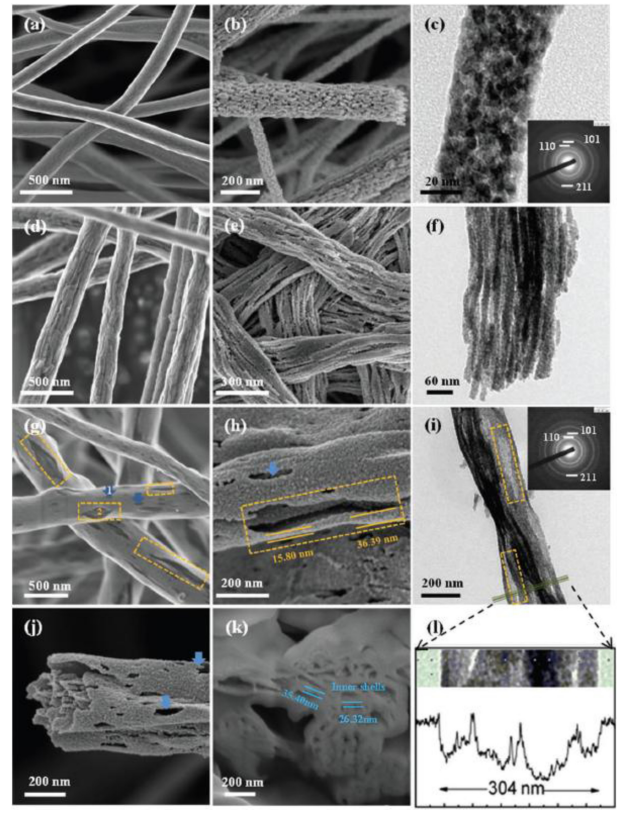

Fig. 6. Image analysis of morphological evolution of as-spun and calcined SnO_2 fibers prepared at different flow rates (a) SEM image of as-spun fibers (5 μL min^{-1}). (b) SEM image of densely packed SnO_2 fibers after calcination at 500°C (5 μL min^{-1}). (c) TEM image of a densely packed SnO_2 fiber (inset shows selected-area diffraction (SAD) pattern of the corresponding fiber). (d) SEM image of as-spun fibers (15 μL min^{-1}). (e) SEM image of multi-fibrous fibers after calcination at 500°C (15 μL min^{-1}). (f) TEM image of a multi-fibrous fiber. (g) SEM image of as-spun fibers (25 μL min^{-1}). Blue arrows (1) indicate small dimples on fibers, and yellow dotted frames (2) show crevices along the longitudinal direction. (h) SEM image of thin-wall assembled SnO_2 fibers after calcination at 500°C (25 μL min^{-1}); blue arrows and yellow dotted frames indicate multiple small and elongated open pores. Yellow parallel lines denote a layer thickness of approximately 30 nm. (i) TEM image of a thin-wall assembled SnO_2 fiber. (j) Magnified SEM image of a broken thin-wall assembled SnO_2 fiber. (k) FIB-cut image of thin-wall assembled SnO_2 fibers. (l) Intensity profile across a thin-wall assembled SnO_2 fiber shown in (i). Adapted from Ref. [1].

regulation and excessive fatty acid oxidation. These fatty acids are converted into ketone bodies in the liver [83-88], which, owing to their high volatility, are readily released through respiration. Studies have shown that the breath acetone concentration in diabetic patients typically exceeds 1.8 ppm—approximately two to six times higher than in healthy individuals (0.3–0.9 ppm) [13,14].

Consequently, for accurate diabetes diagnosis, highly sensitive sensors capable of detecting acetone concentrations below 1 ppm, even under high-humidity conditions (>80% relative humidity) and in the presence of other breath constituents, are essential. Among various high-performance sensing platforms, SnO_2-based nanofiber sensors fabricated via electrospinning have demonstrated distinct advantages for acetone detection due to their large surface area and porous morphology.

In particular, the incorporation of catalytic noble metals such as platinum significantly enhances both the selectivity and sensitivity toward acetone. Clinical studies have shown that these sensors can effectively differentiate between breath samples of diabetic patients and healthy individuals while maintaining stable operation under high-humidity conditions exceeding 80% relative humidity. These findings indicate that chemiresistive gas sensors utilizing breath acetone offer a noninvasive, rapid, and reliable auxiliary tool for the early diagnosis of diabetes.

In the reported study, the researchers controlled the electrospinning flow rate to modulate the structural morphology of the SnO_2 nanofibers. As shown in Figs. 5(a)–(c), during subsequent thermal treatment, the ceramic precursor crystallized while the nonvolatile polymer was removed.

At a low electrospinning flow rate, the resulting fibers exhibited smooth surfaces with homogeneous internal distributions of the polymer and tin precursor. During calcination, the polymer decomposed into CO_2 and water vapor, while the tin precursor crystallized into polycrystalline

SnO_2 nanoparticles.

As the flow rate increased, a marked morphological transformation was observed: the polymer chains within the fibers stretched along the longitudinal axis, producing an elongated internal alignment. When an optimal intermediate flow rate was applied, wrinkled, stripe-like textures appeared along the fiber direction. After heat treatment, a highly porous structure was clearly identified.

Catalytic functionalization with noble Pt nanoparticles was further facilitated by the thin, tubular, and porous surface morphology, allowing uniform dispersion of small Pt particles and efficient coverage over a large surface area.

Scanning electron microscopy (SEM) and transmission electron microscopy (TEM) analyses confirmed the surface morphologies of the nanofibers. Distinct morphological differences in the SnO_2 fibers were observed depending on the electrospinning flow rate, and after calcination, a unique porous architecture emerged due to the crystallization of the tin precursor and the removal of the polymer matrix.

As shown in Figs. 6(g)–(i), fibers fabricated under a high flow rate exhibited numerous elongated open pores and a wrinkled, thin-walled structure, indicating that gas molecules could easily penetrate the entire sensing layer. This morphological trend was further verified by Brunauer–Emmett–Teller (BET) analysis. Unlike the densely packed fibers produced under low-flow conditions, which showed a dominant pore distribution in the 10–30 nm range, the fibers obtained at a high flow rate exhibited a broader pore distribution, primarily exceeding 30 nm, corresponding to the overlapped thin-sheet morphology. These structural features directly influenced gas-sensing performance.

As shown in Fig. 7(b), the sample with a wrinkled, thin-walled structure and broader pore distribution (sample 25) displayed a larger resistance change in response to varying acetone concentrations over time and exhibited a faster response rate, approximately 30 seconds shorter than that of the denser fibers. To further enhance sensing performance, acetone exposure tests were conducted under controlled noble-metal doping concentrations. The results revealed that a 5% Pt doping level yielded the highest sensing response and fastest reaction rate, indicating an optimal balance between catalytic activity and charge-transfer efficiency. In a reference study, the researchers demonstrated diabetes diagnosis through acetone detection, as well as the potential for early lung cancer diagnosis via toluene sensing and concentration monitoring (Figs. 7(d)–(f)) [89]. The sensor exhibited measurable responses to toluene concentrations ranging from 120 to 3 ppm over time. As shown in Fig. 7(e), both pristine and densely packed SnO_2 fibers displayed weak sensitivity toward toluene, whereas Pt-functionalized samples showed a dramatic increase

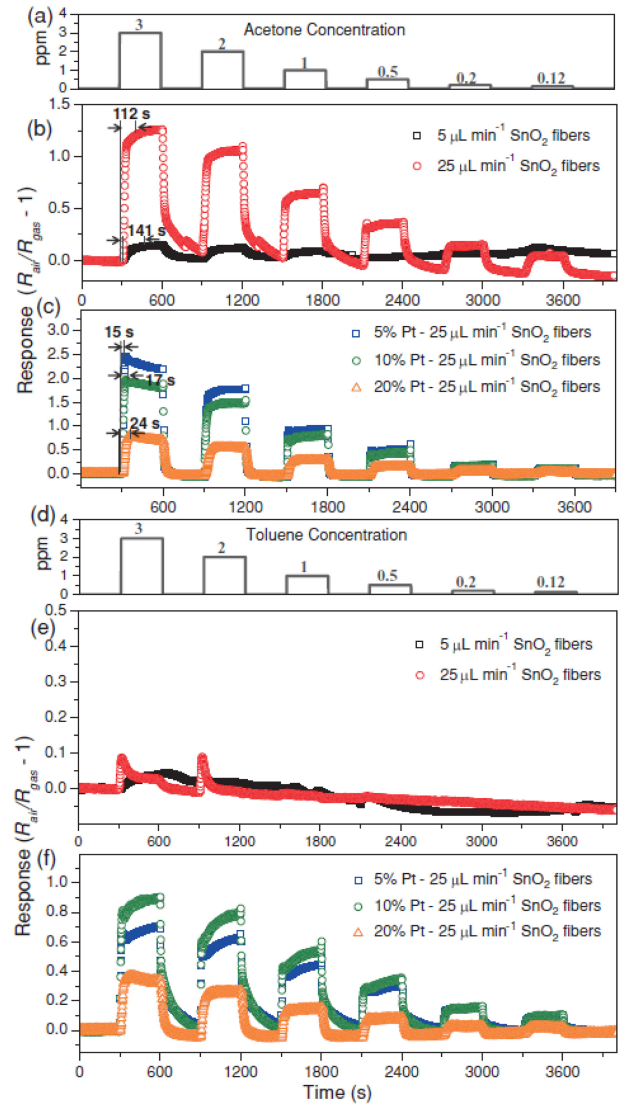

Fig. 7. Dynamic response of SnO_2 fibers to cyclic acetone and toluene concentrations. (a) Cyclic acetone concentrations arranged as 3 ppm, 2 ppm, 1 ppm, 500 ppb, 200 ppb, and 120 ppb over time. Acetone responses of (b) pure SnO_2 fibers synthesized at 5 μL min^{-1} and 25 μL min^{-1} and (c) thin-wall assembled SnO_2 fibers modified with 5 wt%, 10 wt%, and 20 wt% Pt decoration under 80% relative humidity at 300°C. (d) Cyclic toluene concentrations arranged as 3 ppm, 2 ppm, 1 ppm, 500 ppb, 200 ppb, and 120 ppb over time. Toluene responses of (e) pure SnO_2 fibers synthesized at 5 μL min^{-1} and 25 μL min^{-1} and (f) thin-wall assembled SnO_2 fibers modified with 5 wt%, 10 wt%, and 20 wt% Pt decoration under 80% relative humidity at 300°C. Adapted from Ref. [1].

in response (Fig. 7(f)). Therefore, the incorporation of Pt markedly enhanced both the selectivity and sensitivity toward toluene, confirming its critical role in achieving multianalyte detection.

This enhancement was attributed to the chemical sensitization effect of Pt catalysts, which facilitated the

dissociation and oxidation of toluene molecules. Accordingly, Pt decoration imparted distinct toluene selectivity to SnO_2-based sensors.

In the referenced study, the typical SnO_2 structure was modified into nanofibers through flow-rate control during electrospinning, resulting in a maximized surface area that enabled efficient and extensive noble-metal decoration.

Consequently, the sensors exhibited excellent response characteristics, achieving ultrasensitive detection at acetone concentrations relevant to diabetic breath, along with rapid response and recovery times.

The strategy of enhancing sensor performance by maximizing the adsorption of oxygen and target gas molecules is not limited to SnO_2. Through noble-metal functionalization, gas selectivity can be significantly improved, and through nanostructure engineering, response performance can be further optimized, offering a versatile approach to overcoming the intrinsic selectivity limitations of conventional metal oxide semiconductors.

3.1.3 Asthma Diagnosis

Asthma is a chronic respiratory disease characterized by recurrent episodes of dyspnea and wheezing, with severity and frequency varying among individuals. According to the Global Initiative for Asthma (GINA), asthma affects approximately 358 million people worldwide and causes about 495,000 deaths annually [22]. Among the various biomarkers investigated, nitric oxide (NO) and hydrogen sulfide (H_2S) in exhaled breath are recognized as key indicators of airway inflammation associated with asthma [22]. Moreover, H_2S has been identified as a potential biomarker not only for asthma but also for chronic obstructive pulmonary disease (COPD) [90] and halitosis [91-93]. Clinical studies have shown that H_2S concentrations differ according to asthma subtype: eosinophilic asthma exhibits the lowest concentration (7.70 ± 4.20 ppb), while paucigranulocytic asthma shows higher levels (11.1 ± 4.60 ppb). Interestingly, healthy individuals demonstrate even higher H_2S levels (26.9 ± 4.60 ppb), suggesting that elevated exhaled H_2S alone does not directly correlate with disease presence. Building upon these findings, recent studies have developed low-cost, portable, and intelligent diagnostic devices that integrate functional sensors with electronic circuitry to enable real-time, noninvasive asthma detection.

To validate this approach, a research team collected exhaled breath samples from 28 patients with asthma and 28 healthy individuals, confirming that the method could effectively distinguish between the two groups.

To replace costly electrochemical H_2S sensors, the researchers developed a low-cost, portable chemiresistive sensor by doping CuO—a material known for its high H_2S sensitivity—into γ-Bi_2MoO_6, thereby creating an ultra–high-performance H_2S gas sensor. The γ-Bi_2MoO_6 precursor was synthesized via a hydrothermal process, followed by solvent-evaporation–based doping, in which Cu precursors were introduced under controlled concentrations. The mixture was subsequently stirred and calcined.

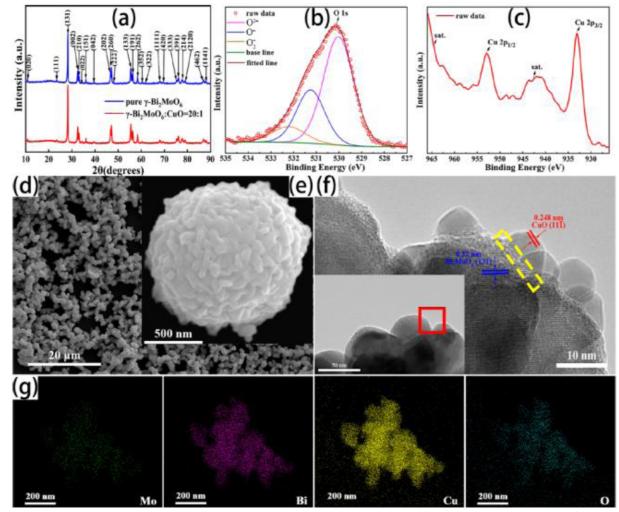

Fig. 8. Structural and chemical characterization of the γ-Bi_2MoO_6-CuO sensor (a) XRD patterns of pristine γ-Bi_2MoO_6 and γ-Bi_2MoO_6 decorated with 5 at% CuO (Sample 2). (b, c) Core-level spectra of O 1s and Cu 2p of Sample 2. (d) Low-magnification SEM image of Sample 2. (e) SEM image of a single γ-Bi_2MoO_6 microsphere (Sample 2). (f) HRTEM image of the interface between CuO and γ-Bi_2MoO_6, captured from the red rectangular area in the inset. (g) EDS mapping of Mo, Bi, Cu, and O elements in Sample 2. Adapted from Ref. [18].

As shown in Fig. 8, X-ray diffraction (XRD) and spectroscopic analyses were performed to elucidate the doping behavior and surface states, while scanning electron microscopy (SEM) and transmission electron microscopy (TEM) analyses confirmed the uniform distribution of Cu dopants and detailed surface morphologies.

Fig. 9 illustrates the sensor response to 100 ppm H_2S at various operating temperatures under controlled concentration conditions. The optimal temperature was identified as 180°C, with the best performance observed for the material doped at 5 at.%. Upon exposure to H_2S, the sensor resistance decreased—a characteristic behavior of n-type metal oxide semiconductors, indicating that the composite followed the n-type conduction of the γ-Bi_2MoO_6 host rather than the p-type nature of the CuO dopant.

To evaluate the medical applicability of the developed sensor, breath-sensing performance and selectivity tests were conducted. For selectivity testing, exhaled breath and reference gases were injected into an airbag and delivered to the sensor. The introduction of NO or acetone caused no appreciable

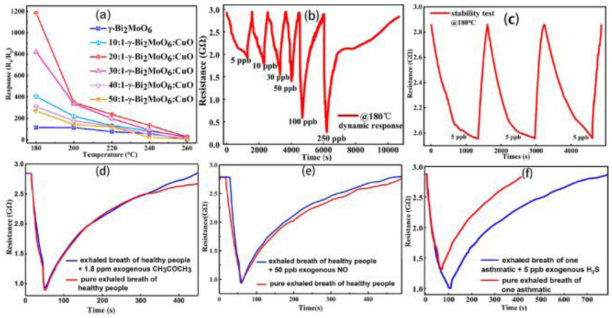

Fig. 9. Gas sensing performance of the sensor. (a) Temperature-dependent response values of sensors based on γ-Bi_2MoO_6–CuO heterostructure materials with varying CuO molar ratios toward 100 ppm exogenous H_2S, tested in static mode. (b) Dynamic resistance variation of Sensor B (γ-Bi_2MoO_6/CuO = 20:1), showing optimal gas-sensing performance toward different concentrations of exogenous H_2S at 180°C. (c) Repeatability and stability test of Sensor B toward 5 ppb exogenous H_2S at 180°C. (d–f) Dynamic responses of Sensor B toward pure exhaled breath (red line) and the same exhaled breath spiked with 1.8 ppm acetone, 50 ppb NO, and 5 ppb H_2S (blue line), respectively. (b–f) were tested in dynamic mode. In (b, c), H_2S gas was diluted in air. Adapted from Ref. [18].

change compared to breath alone, whereas H_2S produced a distinct response shift, demonstrating high selectivity toward H_2S. For clinical validation, all subjects were screened using a bronchodilation test (BDT), after which two cohorts—28 asthma patients and 28 healthy controls—were enrolled, yielding 56 breath samples for sensor evaluation. To exclude confounding H_2S originating from halitosis, nasal sampling was performed instead of oral collection.

Although some overlap existed between the response distributions of the two groups, their mean and variance values enabled clear differentiation: the asthma cohort exhibited a response of 2.39 ± 0.18, whereas the healthy cohort showed a response of 2.90 ± 0.22, indicating higher readings in healthy subjects.

For longitudinal assessment, a single patient was monitored over 5.5 days. As treatment progressed, exhaled H_2S concentrations gradually increased, corresponding to the patient's improvement from severe to milder asthma.

Cross-validation using peak expiratory flow rate and variability confirmed that alleviating airway inflammation through treatment improved airway stability and reduced flow rate variability.

In other words, a decrease in the sensor response value indicated symptom relief and improved inflammation control, consistent with the expected biomarker behavior (Fig. 10).

From a materials perspective, CuO exhibits p-type conductivity owing to copper vacancies. When CuO is doped into the n-type γ-Bi_2MoO_6 host, an interfacial depletion layer

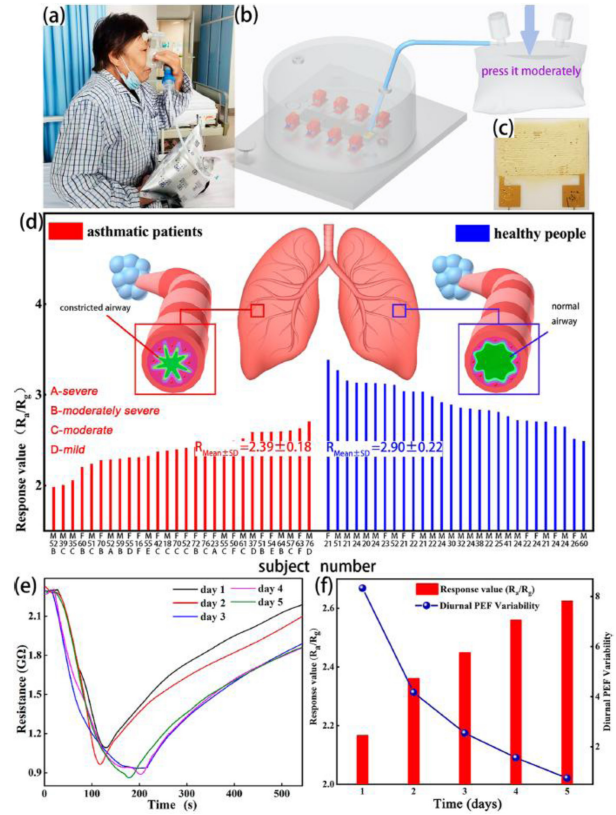

Fig. 10. Clinical experiment. (a) Collection of exhaled breath from an asthmatic patient. (b) Schematic diagram of the exhaled-breath testing process. (c) Photograph of Sensor B. (d) Comparison of response values between exhaled breaths of asthmatic patients and healthy individuals; gender and age are indicated (M: male, F: female). Severity levels are marked A–F according to the BDT results, where E and F denote small airway ventilation dysfunction and normal pulmonary ventilation diagnosed as asthma, respectively. (e) Dynamic response of the sensor to exhaled breath from an inpatient with asthma, collected on different days. (f) Histogram of sensor responses in (e); the line–symbol graph shows D. PEF V. in Table 2. Adapted from Ref. [18].

forms between the p-type dopant and n-type matrix, increasing the baseline resistance. This observation aligns with experimental results showing that the resistance in air is higher for the Cu-doped material than for undoped γ-Bi_2MoO_6.

Oxygen adsorption creates surface states and increases hole concentration; at low H_2S levels, reactions between H_2S and adsorbed oxygen release electrons, which recombine with holes, thinning the depletion layer and decreasing the resistance—representing the proposed sensing mechanism of the material toward H_2S.

To elucidate the mechanism behind the ultrahigh sensitivity, first-principles density functional theory (DFT) calculations were performed. The results indicated that H_2S adsorption on the γ-Bi_2MoO_6 surface had little effect, whereas on the CuO

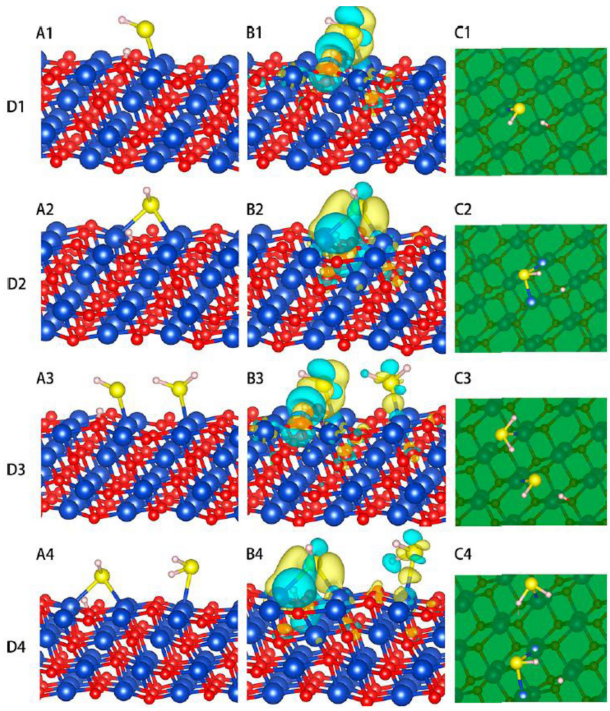

Fig. 11. Atomic geometries of D1, D2, D3, and D4 structures. Yellow, pink, red, and blue spheres represent S, H, O, and Cu atoms, respectively. A (A1–A4) and C (C1–C4) show side and top views, respectively; the green plane represents the CuO surface. B (B1–B4) illustrates the charge density difference of D1–D4, where yellow indicates electron gain and light blue indicates electron loss. Adapted from Ref. [18].

surface, H_2S underwent stable adsorption and dissociation (Fig. 11).

In the initial step, an H_2S molecule dissociated into HS and H, forming strong bonds with Cu and O atoms. A low adsorption energy (−1.47 eV) and substantial charge transfer (~0.34 e^-) were observed, effectively modulating the depletion layer and accounting for the pronounced resistance change and high sensing response. Subsequent H_2S molecules were adsorbed molecularly (without dissociation), forming relatively weaker bonds.

These computational findings support the proposed mechanism, explaining the exceptional sensitivity of the engineered heterojunction sensor to ultralow H_2S concentrations.

In the referenced study, two materials previously recognized for excellent H_2S sensing were integrated into a heterostructured sensor, achieving more than a sixfold enhancement in response. Clinical implementation, including patient recruitment and real-time breath monitoring, confirmed the correlation between symptom relief and decreasing exhaled H_2S levels, demonstrating the sensor's ability to track disease progression. Complementary first-principles calculations elucidated the origin of the high response, providing a consistent mechanistic basis for the observed performance. Collectively, these advances pave the way for portable, user-friendly devices for asthma management, particularly suited for children and older adults.

3.1.4 COVID-19 Diagnosis

Over the past two decades, several highly pathogenic coronavirus variants—including SARS-CoV, MERS-CoV, and the pandemic-causing SARS-CoV-2—have emerged, posing significant threats to global public health [19,20,95-98].

The current gold-standard diagnostic method, reverse transcription quantitative polymerase chain reaction (RT-qPCR), provides high accuracy but has notable limitations. It requires skilled personnel, expensive equipment, invasive sampling procedures, and long analysis times, which restrict its use for large-scale and rapid screening [99-101]. Although auxiliary diagnostic methods such as clinical symptom evaluation, imaging, and blood analysis have been employed to complement RT-qPCR, they remain inadequate for high-throughput population screening [102-105]. Because COVID-19 primarily affects the respiratory system, breath-based diagnosis has emerged as a promising alternative that is noninvasive, rapid, and comfortable for patients [106]. Exhaled breath contains volatile organic compounds (VOCs), such as acetone and methanol, whose compositional changes can serve as metabolic biomarkers of infection. However, despite their high precision, analytical tools such as gas chromatography–mass spectrometry (GC–MS) are constrained by high cost, long analysis times, and the need for trained personnel, limiting their practicality for point-of-care COVID-19 screening.

The VOCs produced within the respiratory tract of COVID-19 patients vary dynamically with virus–host interactions and disease progression. These evolving VOC profiles can be effectively tracked through pattern recognition using an electronic nose (e-nose) system. The e-nose, previously applied to detect respiratory diseases such as pneumonia, tuberculosis, and renal failure, has also been used for pre-screening COVID-19 prior to confirmatory testing [107-110].

One study attempted to detect COVID-19 through parts-per-million (ppm) level detection of CO, acetone, and alcohol using commercial metal-oxide-semiconductor (MOS) sensors such as MQ-135 and MQ-2, suggesting their potential application in infectious disease diagnostics [36,111]. Recent reviews have emphasized that improving diagnostic accuracy requires integrating multiple MOS-based gas sensors and electrochemical sensors into e-nose platforms to enable real-time, multiplexed monitoring of breath biomarkers [36,111].

Building on this concept, a research team made the first

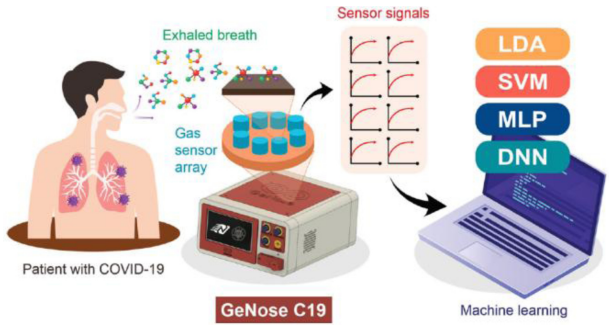

Fig. 12. Illustration of fast and noninvasive COVID-19 detection using the portable electronic nose (GeNose C19) integrated with artificial intelligence (AI). Four machine learning algorithms—LDA, SVM, MLP, and DNN—were employed to differentiate and classify the exhaled breath patterns of patients, as measured by ten different metal oxide semiconductor gas sensors. Adapted from Ref. [5].

clinical attempt to identify COVID-19 patients using an e-nose system. They developed a portable breath analyzer, GeNose C19, which integrates an MOS-based gas sensor array, a machine-learning analysis module, and a standardized breath-sampling setup (Fig. 12). Clinical validation was conducted in two hospitals in Indonesia, where subjects confirmed positive or negative by RT-qPCR provided exhaled breath samples. The resulting breath profiles were analyzed to evaluate the system's ability to discriminate between infected and healthy individuals.

To maximize classification accuracy, four machine-learning algorithms were compared to identify the optimal configuration for the device. The GeNose C19 analyzer consists of two main units: a sensor module and a breath-sampling module (Figs. 13(a) and (b)). The sampling unit employs a disposable breath bag equipped with a HEPA filter and a moisture-absorption layer to eliminate viral aerosols and minimize humidity interference (Figs. 13(c)–(f)). Breath collection follows an end-tidal sampling protocol to avoid oral contamination and to better reflect blood-borne VOCs [112].

The HEPA filter was verified by RT-qPCR to effectively remove SARS-CoV-2 RNA, ensuring safety for both patients and clinical staff [69,70]. The sensor module comprises an array of ten MOS-based sensors (S1–S10) and environmental sensors. It operates under a reproducible three-stage sequence (purge–sample–recovery) controlled by a micropump and valves.

The sequence begins with a 10 s delay phase to establish the baseline, followed by a 40 s sampling phase to record resistance changes to the breath sample, and ends with a 120 s purge phase to restore the sensors to baseline conditions.

Because GeNose C19 is sensitive to ambient conditions such as humidity and background odors, preconditioning steps,

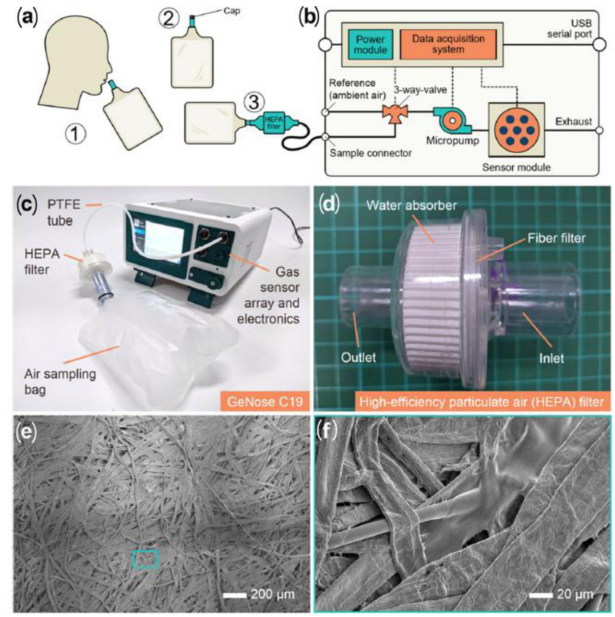

Fig. 13. Integrated GeNose C19 system and its components. (a) Schematic of the off-line breath sampling process for GeNose C19: (1) air is inhaled through the nose and exhaled through the mouth into a sampling bag, (2) the bag cap is sealed to prevent air leakage, and (3) the sampling bag is directly connected to the electronic nose inlet (sample connector). (b) Diagram and (c) photograph of the GeNose C19 integrated with a high-efficiency particulate air (HEPA) filter and an air sampling bag through a flexible, medical-grade polytetrafluoroethylene (PTFE) tube with an outer diameter of 4 mm. The electronic nose comprises several major electronic and mechanical components, including a power module, data acquisition system, three-way valve, micropump, and a sensor module enclosed in a sealed gas chamber. The sensor module consists of an array of ten distinct sensing devices. (d) HEPA filter used to remove particulate matter and capture SARS-CoV-2 from the exhaled breath of COVID-19–positive patients. (e, f) Scanning electron micrographs of the fiber filter used in the GeNose C19 filtering system. Adapted from Ref. [5].

including environmental adjustment, device warm-up, and patient fasting, are necessary to ensure stability and reproducibility.

In clinical operation, raw breath signals from RT-qPCR-positive and RT-qPCR-negative subjects cannot be directly distinguished (Figs. 14(a) and (b)). To overcome this limitation, 40 statistical features—including the maximum, median, standard deviation, and variance from each channel—were extracted from the sensor array signals. Statistical analysis revealed significant differences ($p < 0.05$) between positive and negative groups for sensors S1, S5, S6, S9, and S10 (Figs. 14(c)–(f)), indicating that the array outputs could be effectively used for machine-learning–based classification.

Clinical profiling of GeNose C19 was conducted with 83

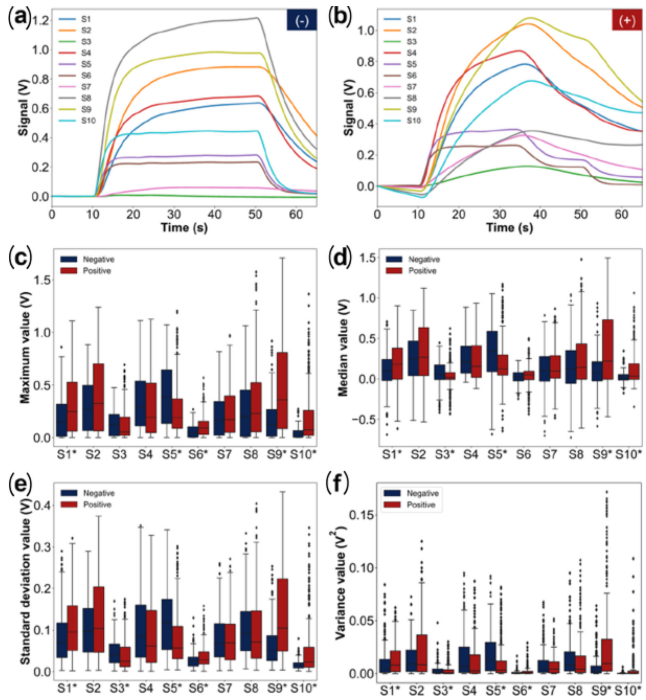

Fig. 14. GeNose C19 sensor responses and extracted features from the exhaled breaths of RT-qPCR-confirmed COVID-19–negative and –positive patients. Typical sensing responses were obtained from ten conductometric gas sensors (S1–S10) integrated into the portable GeNose C19 system for the exhaled breaths of RT-qPCR-confirmed (a) negative and (b) positive COVID-19 patients. Boxplots show the distribution of extracted features for negative and positive samples, including (c) maximum, (d) median, (e) standard deviation, and (f) variance values. Adapted from Ref. [5].

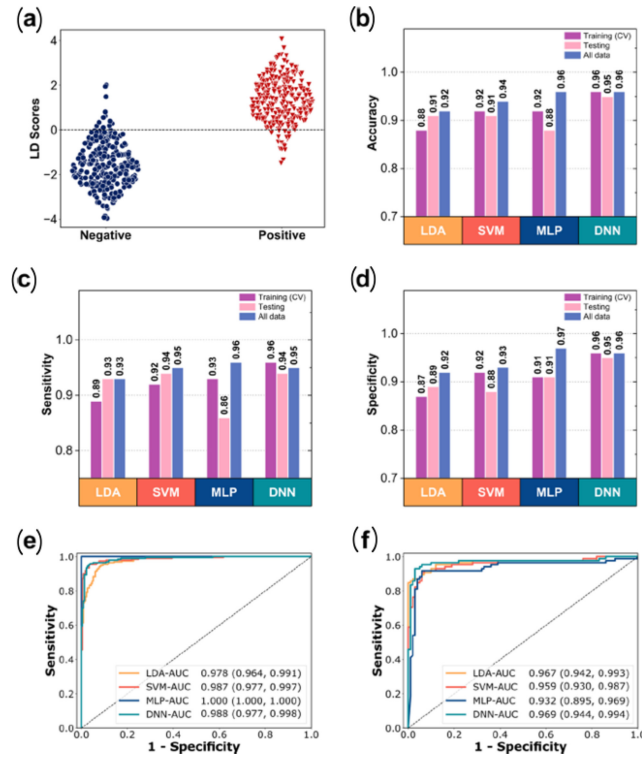

Fig. 15. Measured breath data analysis using machine learning. (a) Classification of exhaled breath samples (positive and negative COVID-19) using the LDA model. (b) Overall accuracy (micro-averaged F1-score), (c) sensitivity, and (d) specificity for the training (10-fold cross-validation), testing, and overall datasets, obtained from four machine learning algorithms (LDA, SVM, MLP, and DNN). (e, f) Receiver operating characteristic (ROC) curves of the training and testing datasets, respectively, using the same four algorithms. The AUC and confidence intervals are also presented. Adapted from Ref. [5].

participants (43 RT-qPCR-positive and 40 RT-qPCR-negative for COVID-19) across two hospitals in Indonesia. From 615 collected breath samples, valid samples (n = 333 and n = 282) were analyzed. Most subjects were asymptomatic (~80%) or exhibited mild symptoms. The dataset was split 70:30 for training and validation, and four supervised learning algorithms—linear discriminant analysis (LDA), support vector machine (SVM), multilayer perceptron (MLP), and deep neural network (DNN)—were evaluated.

Among these models, the DNN demonstrated the most stable and highest performance, achieving a sensitivity of 95.5%, a specificity of 95.7%, and an area under the curve (AUC) of 95.6%. The small difference between training and test performance suggested minimal overfitting, consistent with the ROC curves (Fig. 15). By contrast, several tree-based models, such as gradient boosting and decision trees, exhibited higher overfitting tendencies. Overall, supervised classification enabled statistically significant separation of breath patterns between RT-qPCR-positive and RT-qPCR-negative groups, supporting the clinical utility of GeNose C19 for reliable COVID-19 pre-screening in practical settings.

In summary, to address the diagnostic challenges of RT-qPCR—including high cost, invasiveness, and long turnaround times—GeNose C19 was developed as a portable breath analyzer that integrates an MOS-based sensor array with a DNN-driven pattern recognition module. Using an end-tidal breath collection system equipped with a HEPA filter and moisture-absorption layer, the device ensured both viral safety and signal reliability. In clinical testing, the DNN model achieved 95.5% sensitivity and 95.7% specificity, enabling robust classification of RT-qPCR-positive and -negative subjects. These results demonstrate the practical feasibility of a low-cost, portable e-nose platform for large-scale, rapid pre-screening of COVID-19 and other respiratory infections in clinical environments. Furthermore, the establishment of a standardized breath-sampling protocol underscores the importance of sample preprocessing in achieving reliable and reproducible breath analysis.

3.2 Cutaneous VOC–Based Diagnosis

The noninvasive assessment of human health is one of the central goals of modern medical research. Achieving this requires establishing a link between internal physiological states and externally measurable signals, among which gases emitted by the human body serve as key indicators. The relationship between exhaled breath and disease has been extensively studied: ammonia is a known biomarker of renal dysfunction, acetone indicates diabetes, and nitrogen oxides are associated with asthma [113-116].

Beyond exhaled breath, the human body also releases gases through the skin. In traditional medical practices, such as Oriental medicine, body odor has long been regarded as a diagnostic cue [117]. For example, nonenal has been identified in the skin gas of elderly individuals, and postmortem analyses have characterized distinctive odor components [118,119]. However, systematic studies on the composition of skin gases in healthy young individuals or on the anatomical regions that emit the highest levels of gas remain limited. Research employing gas sensors to analyze skin-emitted volatile organic compounds (VOCs) is still in its early stages. This context underscores the potential of skin-emitted gases as a novel, noninvasive diagnostic pathway and has motivated ongoing efforts to identify disease-specific skin VOC patterns and detect them using portable gas-sensing platforms [9].

3.2.1 Tuberculosis Diagnosis

Tuberculosis (TB) remains a major global health challenge, with approximately 95% of cases occurring in developing countries and an estimated one-third of the world's population harboring latent TB infections [120,121]. Latent TB carries a lifetime risk of 5–10% of progressing to active disease, a risk that is substantially increased by HIV coinfection, smoking, and malnutrition, thereby accelerating TB transmission [120,121]. Diagnosis is particularly challenging in children and people living with HIV, leading to an estimated 3 million undiagnosed active TB cases worldwide each year [22,122]. This diagnostic gap arises from the nonspecific clinical manifestations of TB and the limitations of existing diagnostic methods regarding turnaround time, sensitivity, specificity, and cos [21]. For instance, sputum smear microscopy costs USD 2.6–10.5 but has a sensitivity of only 20–80%, while culture methods can require 4–8 weeks, delaying diagnosis and treatment initiation [123,124]. Sensitivity is even lower in HIV-positive and extrapulmonary TB cases [21].

The GeneXpert MTB/RIF assay, the fastest and most widely used molecular diagnostic test, can deliver results within two hours, yet its sensitivity is only 88% as an initial diagnostic test and 67% for smear-negative cases [125]. Moreover, the high costs of instruments and cartridges, along with requirements for stable power, security, and regular calibration, hinder its implementation in resource-limited settings [126].

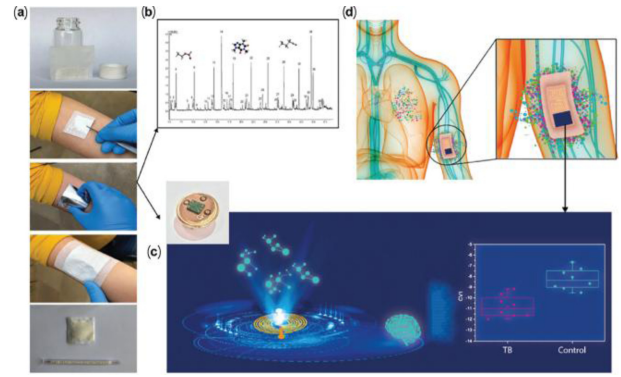

Fig. 16. Study schematic. (a) Skin headspace sampling procedure using poly(2,6-diphenylphenylene oxide) polymer. Samples were transferred into glass tubes for two types of analyses: (b) GC-MS analysis and (c) nanomaterial-based sensor array combined with machine learning analysis. (d) Wearable device applied directly to the skin. Adapted from Ref. [9].

These challenges underscore the urgent need for new diagnostic technologies that combine low cost and high accuracy. Early diagnosis and prompt treatment initiation can significantly reduce morbidity and transmission. The global economic burden of TB, including productivity losses and mortality, is estimated at approximately USD 12 billion annually [127,128]. In response to these limitations, a research team proposed and implemented a biomedical device for noninvasive TB detection using a sensor array and machine-learning–based analysis.

The team targeted TB-associated VOCs collected from the air immediately above the skin surface, hypothesizing that distinct concentration patterns compared to healthy individuals could indicate active infection or high-risk status. To enable point-of-care application, they developed a flexible, wearable polymer pouch capable of collecting and storing skin-emitted VOCs, which was integrated with a nanomaterial-based sensor array and machine-learning analytics.

The study comprised three offline phases—skin gas collection, GC–MS analysis, and nanomaterial sensor analysis with machine learning) followed by one online validation phase using a wearable device in situ.

Offline clinical studies were conducted in Cape Town, South Africa, and New Delhi, India, involving 320 and 316 participants, respectively (total n = 636; ages 22–60 years). Twelve potential confounders, including HIV status and smoking habits, were monitored. Sampling was performed on the forearm and chest using two porous polymer pouches made of poly(2,6-diphenylphenylene oxide) and two

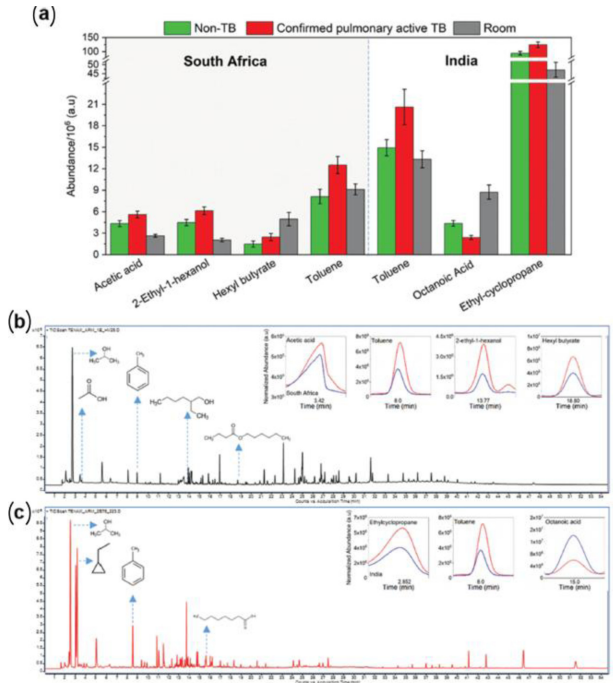

Fig. 17. GC-MS results. Samples from South Africa included 89 confirmed pulmonary active TB patients, 90 non-TB healthy controls, and 262 room samples. Samples from India included 89 confirmed pulmonary active TB patients, 193 non-TB healthy controls, and 193 room samples. (a) Abundance of toluene, acetic acid, 2-ethyl-1-hexanol, ethyl-cyclopropane, hexyl butyrate, and octanoic acid among confirmed TB patients, non-TB controls, and room samples from both sites. Two extreme outliers were excluded for hexyl butyrate among confirmed TB patients. (b, c) Representative chromatograms showing statistically significant VOCs and isopropyl alcohol (IPA) as a skin-cleaning component from South Africa and India, respectively. Insets show representative chromatograms of relevant VOCs based on total ion count traces. Error bars indicate standard errors. The Steel method was used for post hoc testing with $\alpha = 0.05$ compared to the TB group. Adapted from Ref. [9].

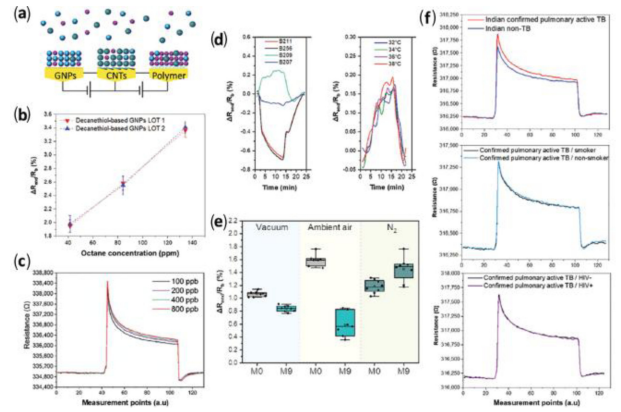

Fig. 18. Sensor array responses. (a) Schematic illustration of a sensor array. (b) Representative responses of decanethiol-capped GNP sensors from two batches toward increasing octane concentrations. (c) Representative response of the same sensor toward increasing toluene concentrations. (d) Response rate to 0.6 ppb toluene in nitrogen for sensors with different thiol ligands at 34°C (left) and the temperature effect on sensor response of decanethiol (B209)-based GNPs exposed to 1.2 ppm toluene (right). (e) Representative responses of dodecanethiol-based GNPs toward 1-methylnaphthalene at 272 ppb in nitrogen under different storage conditions at the starting point (M0) and after nine months (M9). (f) Representative signals of the same sensor for confirmed pulmonary active TB and non-TB skin samples collected from the clinical site in India, including TB patients with and without smoking habits and HIV infection. Adapted from Ref. [9].

polydimethylsiloxane (PDMS) sheets affixed with medical tape (Fig. 16) [129].

Indoor-air controls were collected in the same manner to evaluate exogenous VOC contributions. The collected skin-emitted VOCs were then analyzed qualitatively and quantitatively using GC–MS.

Each compound was detected in more than 80% of all samples, supporting its potential role as a TB-related biomarker. Because GC–MS is unsuitable for point-of-care diagnostics, it was used as a reference method to elucidate the relationships between metabolic pathways and VOCs and to optimize the nanomaterial sensor algorithms.

In the Cape Town cohort, the study evaluated 89 patients with TB, 90 healthy controls, and 262 indoor-air controls, identifying four VOCs significantly enriched in the TB-positive group: toluene (retention time 8.4 min), acetic acid (3.34 min), 2-ethyl-1-hexanol (13.7 min), and hexyl butyrate (18.8 min). In the New Delhi cohort, which included 89 TB patients, 193 healthy controls, and 193 indoor-air controls, three VOCs were enriched in TB-positive subjects: toluene (8.4 min), ethyl cyclopropane (2.8 min), and octanoic acid (15.2 min). Notably, toluene exhibited the most significant elevation in both countries (Fig. 17). Although toluene can be an exogenous compound associated with petrochemical exposure [25], its concentration showed clear case–control differences in both cohorts when compared with indoor-air controls. Using 22 sensors (yielding 43 features), quadratic discriminant function analysis (QDFA) achieved 84% accuracy, 90.3% sensitivity, 80.3% specificity, and an area under the curve (AUC) of 0.92 during the training phase. In the 30% blind test subset, performance remained strong, with 87.4% accuracy, 90.4% sensitivity, and 85.7% specificity, demonstrating robust classification capability (Fig. 18).

These results meet the World Health Organization (WHO) criteria for sputum-based tuberculosis testing (sensitivity >90%; specificity >70%).

In subgroup analyses of QFT-positive/HIV-negative participants, the model achieved 91.6–93.8% sensitivity, 70.4–71.2% specificity, and 78.4–81.1% accuracy, indicating its

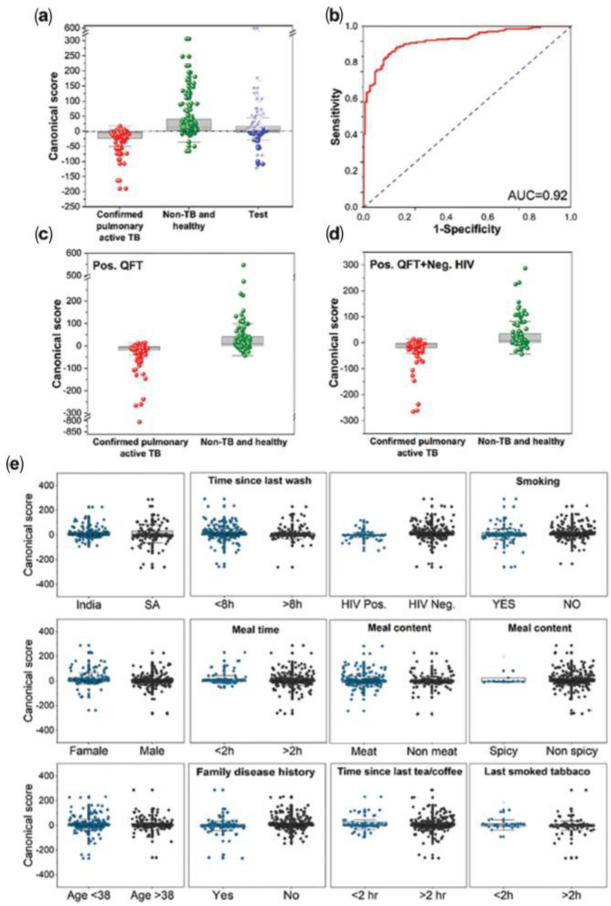

Fig. 19. Quadratic DFA results of the global classifier. (a) Boxplot of canonical scores, where each point represents a sample. The central dashed line denotes Youden's cut-point. Samples above the cut-point are classified as non-TB or healthy, while those below are classified as confirmed pulmonary active TB. Non-TB and healthy test samples are shown as open circles, and confirmed TB samples as filled circles. (b) Receiver operating characteristic (ROC) curve of the model. (c) Boxplot of canonical scores for the subpopulation with QuantiFERON-TB Gold (QFT)-positive status. (d) Boxplot of canonical scores for the subpopulation with QFT-positive and HIV-negative status. (e) Boxplots of canonical scores for confounding factors. Adapted from Ref. [9].

potential to distinguish active TB from latent infection. Furthermore, factors such as sex, HIV status, and smoking habits did not significantly affect the classification outcomes (Fig. 19).

In the final phase, an online real-time diagnostic assessment was performed using a wearable sensor platform. In Riga, Latvia, eight nanomaterial-based sensor devices were affixed to the chests and forearms of 29 healthy participants and 18 patients with active pulmonary TB. Under leave-one-out cross-validation, the system achieved 94.4% sensitivity, 86.2% specificity, and 89.4% accuracy, demonstrating that skin-gas–based sensing can effectively detect tuberculosis in point-of-care environments (Fig. 20).

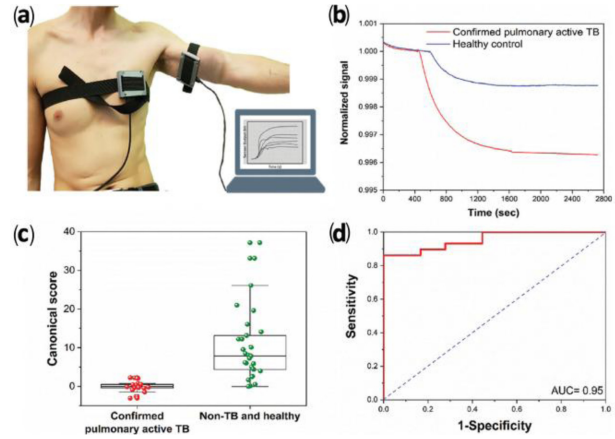

Fig. 20. Wearable device for TB diagnosis. (a) Wearable devices placed on the chest and anterior arm of a volunteer. (b) Representative normalized signals from a sensor in the wearable device attached to the anterior arm. The plotted signal represents normalized resistance relative to the baseline before the patch was attached. (c) Boxplot of canonical scores from the linear DFA model, with each point representing one sample. (d) ROC curve of the model (AUC = area under the curve). Adapted from Ref. [9].

4. CONCLUSION

This review provides a comprehensive overview of recent advances in noninvasive disease diagnostics using chemiresistive metal-oxide semiconductor (MOS) gas sensors. Central to these developments is the recognition that volatile organic compound (VOC) patterns present in exhaled breath and skin emissions reflect the pathophysiological changes associated with disease. The precision and interpretability of large analytical instruments are increasingly being complemented—and, in certain applications, approximated—by portable sensor platforms integrated with pattern recognition and machine learning techniques.

In particular, assembling sensor arrays (electronic noses) with distinct sensing layers and integrating AI-based pattern recognition, including deep neural networks (DNNs), has enabled reliable classification of disease-specific breathprint patterns from complex mixtures of VOCs in exhaled breath and skin emissions [56-61]. Case studies on COVID-19 and tuberculosis further demonstrated that such e-nose systems have strong clinical potential as rapid, low-cost point-of-care (POC) screening tools [5,9].

Despite these promising results, gas sensor platforms have yet to achieve broad clinical and field deployment due to three major bottlenecks. First, although many clinical studies favor offline breathbag collection for safety and operational convenience, the associated sampling, transport, and injection procedures vary across studies, hindering standardization and

limiting real-time diagnostics. Additional sources of error—including bag material, storage time, humidity fluctuations, dilution effects, inter-instrument variability, and long-term drift—require rigorous control. Second, substantial confounders such as diet, smoking, medications, and environmental VOCs, as well as site-specific factors, undermine generalizability. Models trained and validated at a single institution may not reproduce their performance across different hospitals, populations, or environmental conditions. Without multicenter external validation, algorithmic robustness cannot be ensured. Third, from a regulatory standpoint, the absence of standardized breath-sampling and data-interpretation protocols weakens the reproducibility and comparability of evidence for safety and effectiveness, delaying medical device approval. Even after approval, clinical adoption—such as hospital integration and reimbursement listing—remains impeded by the lack of established standards [3,5,9].

Addressing these issues requires integrated co-design and optimization across materials, systems, and software, rather than parallel, isolated progress in each area [69,70,130]. On the sampling side, evidence-based protocols covering acquisition modality, flow-rate control, and confounder management must be established and validated to support generalizable practice. On the materials side, sensor and device architectures should be optimized for reproducible responses and long-term stability under conditions relevant to large-scale manufacturing and prolonged field use [1,18]. At the system level, portability and repeat-measurement efficiency can be improved through low-temperature operation, low-power microheaters, optimized pump and valve sequences, integrated sampling modules, and automated self-cleaning routines. For data and algorithms, standardization of preprocessing and feature engineering—combined with transfer learning, domain adaptation, and explainable AI (XAI)—should be pursued to enhance model reliability and interpretability. Federated learning can further preserve raw data at each clinical site while training a shared model, improving generalization. Personalization and institutionalization strategies can help correct distribution shifts across individuals and centers. Implementing secure aggregation, differential privacy, and encrypted data transmission ensures both regulatory compliance and patient data protection, while maintaining performance [130-133]. Clinically, multicenter external validation, longitudinal follow-up, and thresholding based on within-subject variability are essential for aligning sensor workflows with real-world care pathways.

In summary, chemiresistive gas sensors are emerging as promising platforms for noninvasive and rapid disease screening and monitoring. The convergence of nanostructure engineering, e-nose-based pattern recognition, and standardized clinical workflows is expected to accelerate their clinical translation. Remaining priorities include standardization, model generalization, and long-term stability. Once these challenges are addressed, e-nose-based diagnostics are poised to play an increasingly significant role in personalized health screening and continuous monitoring.

CRediT Authorship Contribution Statement

Jung-Won An: Investigation, Methodology, Writing–original draft. **Ho Won Jang:** Writing–review and editing, Supervision. **Ji-Soo Jang:** Writing–review and editing, Supervision, Funding acquisition.

Declaration of Competing Interest

The authors declare that they have no competing financial interests or personal relationships that may have influenced the work reported in this study.

Acknowledgements

This work was supported by the National Research Foundation of Korea (NRF), funded by the Korean government (MSIT) (grant number RS-2024-00333848); the Korea Institute of Science and Technology (grant numbers 2E33811, 2V10571, and 2N80200); the National Research Foundation of Korea (NRF), funded by the Ministry of Education (grant number 2021R1A6A3A14038599); the Korean Government (MSIT) (grant number RS-2024-00333848); and the Technology Innovation Program (Development of Heterogeneous Multi-Sensor Micro-System Platform), funded by the Ministry of Trade, Industry & Energy (MOTIE, Korea) (grant number 00144157).

REFERENCES

[1] J. Shin, S.J. Choi, I. Lee, D.Y. Youn, C.O. Park, J.H. Lee, et al., Thin-wall assembled sno2 fibers functionalized by catalytic pt nanoparticles and their superior exhaled-breath-sensing properties for the diagnosis of diabetes, Adv. Funct. Mater. 23 (2013) 2357–2367.

[2] W.-L. Chang, C.-C. Chang, Y.-T. Lee, A. D. T. Thi, C.-C. Chen, H.-F. Meng, et al., Gas emission from human skin positions detected by vertical-channel organic semiconductor sensor, Sens. Actuators B Chem. 343 (2021) 129994.

[3] G. Peng, U. Tisch, O. Adams, M. Hakim, N. Shehada, Y.Y. Broza, et al., Diagnosing lung cancer in exhaled breath using gold nanoparticles, Nat. Nanotechnol. 4 (2009) 669–673.

[4] S.J. Choi, L. Persano, A. Camposeo, J.S. Jang, W.T. Koo, S.J. Kim, et al., Electrospun nanostructures for high performance chemiresistive and optical sensors, Macromol. Mater. Eng. 302 (2017) 1600569.

[5] D.K. Nurputra, A. Kusumaatmaja, M.S. Hakim, S.N.

Hidayat, T. Julian, B. Sumanto, et al., Fast and noninvasive electronic nose for sniffing out covid-19 based on exhaled breath-print recognition, NPJ Digit. Med. 5 (2022) 115.
[6] D.M. Cutler, Are we finally winning the war on cancer?, J. Econ. Perspect. 22 (2008) 3–26.
[7] J. Baumbach, W. Vautz, V. Ruzsanyi, L. Freitag, Metabolites in human breath: Ion mobility spectrometers as diagnostic tools for lung diseases, in: A. Amann, D. Smith (Eds.), Breath Analysis for Clinical Diagnosis and Therapeutic Monitoring, World Scientific, Singapore, 2005, pp. 53–66.
[8] C.F. Kneepkens, G. Lepage, C.C. Roy, The potential of the hydrocarbon breath test as a measure of lipid peroxidation, Free Radic. Biol. Med. 17 (1994) 127–160.
[9] R. Vishinkin, R. Busool, E. Mansour, F. Fish, A. Esmail, P. Kumar, et al., Profiles of volatile biomarkers detect tuberculosis from skin, Adv. Sci. 8 (2021) 2100235.
[10] H. O'neill, S. Gordon, M. O'neill, R. Gibbons, J. Szidon, A computerized classification technique for screening for the presence of breath biomarkers in lung cancer, Clin. Chem. 34 (1988) 1613–1618.
[11] H. Yu, L. Xu, M. Cao, X. Chen, P. Wang, J. Jiao, et al., Detection volatile organic compounds in breath as markers of lung cancer using a novel electronic nose, Proceedings of SENSORS, 2003 IEEE, Toronto, Canada, 2003, pp. 1333–1337.
[12] M. Phillips, K. Gleeson, J.M.B. Hughes, J. Greenberg, R.N. Cataneo, L. Baker, et al., Volatile organic compounds in breath as markers of lung cancer: A cross-sectional study, Lancet 353 (1999) 1930–1933.
[13] S. Ryabtsev, A. Shaposhnick, A. Lukin, E. Domashevskaya, Application of semiconductor gas sensors for medical diagnostics, Sens. Actuators B Chem. 59 (1999) 26–29.
[14] C. Deng, J. Zhang, X. Yu, W. Zhang, X. Zhang, Determination of acetone in human breath by gas chromatography–mass spectrometry and solid-phase microextraction with on-fiber derivatization, J. Chromatogr. B 810 (2004) 269–275.
[15] A. Banerjee, P. Rabbitts, J. George, Lung cancer• 3: Fluorescence bronchoscopy: Clinical dilemmas and research opportunities, Thorax 58 (2003) 266.
[16] A.T. Guntner, S. Abegg, K. Konigstein, P.A. Gerber, A. Schmidt-Trucksass, S.E. Pratsinis, Breath sensors for health monitoring, ACS Sens. 4 (2019) 268–280.
[17] C. Cortesia, C. Vilchèze, A. Bernut, W. Contreras, K. Gómez, J. De Waard, et al., Acetic acid, the active component of vinegar, is an effective tuberculocidal disinfectant, MBio 5 (2014) e00013–00014.
[18] Q. Jing, C. Gong, W. Bian, Q. Tian, Y. Zhang, N. Chen, et al., Ultrasensitive chemiresistive gas sensor can diagnose asthma and monitor its severity by analyzing its biomarker h2s: An experimental, clinical, and theoretical study, ACS Sens. 7 (2022) 2243–2252.
[19] N. Zhu, D. Zhang, W. Wang, X. Li, B. Yang, J. Song, et al., A novel coronavirus from patients with pneumonia in china, 2019, N. Engl. J. Med. 382 (2020) 727–733.
[20] K. Dhama, S. Khan, R. Tiwari, S. Sircar, S. Bhat, Y.S. Malik, et al., Coronavirus disease 2019–covid-19, Clin. Microbiol. Rev. 33 (2020) e00028–20.
[21] World Health Organization (WHO), World health statistics 2008, World Health Organization, Geneva, Switzerland, 2008.
[22] Global Initiative for Asthma (GINA), Global strategy for asthma management and prevention (2021 update), Global Initiative for Asthma, Fontana, USA, 2021.
[23] F. Di Pietrantonio, M. Benetti, D. Cannatà, E. Verona, A. Palla-Papavlu, J. Fernández-Pradas, et al., A surface acoustic wave bio-electronic nose for detection of volatile odorant molecules, Biosens. Bioelectron. 67 (2015) 516–523.
[24] R. Roto, A. Rianjanu, A. Rahmawati, I.A. Fatyadi, N. Yulianto, N. Majid, et al., Quartz crystal microbalances functionalized with citric acid-doped polyvinyl acetate nanofibers for ammonia sensing, ACS Appl. Nano Mater. 3 (2020) 5687–5697.
[25] A. Rianjanu, T. Julian, S.N. Hidayat, N. Yulianto, N. Majid, I. Syamsu, et al., Quartz crystal microbalance humidity sensors integrated with hydrophilic polyethyleneimine-grafted polyacrylonitrile nanofibers, Sens. Actuators B Chem. 319 (2020) 128286.
[26] T. Julian, S.N. Hidayat, A. Rianjanu, A.B. Dharmawan, H.S. Wasisto, K. Triyana, Intelligent mobile electronic nose system comprising a hybrid polymer-functionalized quartz crystal microbalance sensor array, ACS omega 5 (2020) 29492–29503.
[27] K. Triyana, A. Rianjanu, D.B. Nugroho, A.H. As' ari, A. Kusumaatmaja, R. Roto, et al., A highly sensitive safrole sensor based on polyvinyl acetate (pvac) nanofiber-coated qcm, Sci. Rep. 9 (2019) 15407.
[28] H.S. Wasisto, S. Merzsch, E. Uhde, A. Waag, E. Peiner, Handheld personal airborne nanoparticle detector based on microelectromechanical silicon resonant cantilever, Microelectron. Eng. 145 (2015) 96–103.
[29] H.S. Wasisto, S. Merzsch, A. Waag, E. Uhde, T. Salthammer, E. Peiner, Airborne engineered nanoparticle mass sensor based on a silicon resonant cantilever, Sens. Actuators B Chem. 180 (2013) 77–89.
[30] A. Rianjanu, S.N. Hidayat, N. Yulianto, N. Majid, K. Triyana, H.S. Wasisto, Sensitivity prediction and analysis of nanofiber-based gas sensors using solubility and vapor pressure parameters, Jpn. J. Appl. Phys. 60 (2021) 107001.
[31] A. Rianjanu, F. Fauzi, K. Triyana, H.S. Wasisto, Electrospun nanofibers for quartz crystal microbalance gas sensors: A review, ACS Appl. Nano Mater. 4 (2021) 9957–9975.
[32] S.Y. Park, Y. Kim, T. Kim, T.H. Eom, S.Y. Kim, H.W. Jang, Chemoresistive materials for electronic nose: Progress, perspectives, and challenges, InfoMat 1 (2019) 289–316.
[33] L. Utari, N.L.W. Septiani, Suyatman, Nugraha, L.O. Nur, H.S. Wasisto, B. Yuliarto, Wearable carbon monoxide sensors based on hybrid graphene/zno nanocomposites, IEEE Access 8 (2020) 49169–49179.
[34] O. Casals, N. Markiewicz, C. Fabrega, I. Gràcia, C. Cané, H.S. Wasisto, et al., A parts per billion (ppb) sensor for no2 with microwatt (μw) power requirements based on micro light plates, ACS Sens. 4 (2019) 822–826.

[35] N. Markiewicz, O. Casals, C. Fabrega, I. Gràcia, C. Cané, H.S. Wasisto, et al., Micro light plates for low-power photoactivated (gas) sensors, Appl. Phys. Lett. 114 (2019) 053508.
[36] T.C. Miller, S.D. Morgera, S.E. Saddow, A. Takshi, M. Palm, Electronic nose with detection method for alcohol, acetone, and carbon monoxide in coronavirus disease 2019 breath simulation model, IEEE Sens. J. 21 (2021) 15935–15943.
[37] O. Qomaruddin, O. Casals, H.S. Wasisto, A. Waag, J.D. Prades, C. Fabrega, Visible-light-driven room temperature no2 gas sensor based on localized surface plasmon resonance: The case of gold nanoparticle decorated zinc oxide nanorods (zno nrs), Chemosensors. 10 (2022) 28.
[38] L. Engel, I. Benito-Altamirano, K.R. Tarantik, C. Pannek, M. Dold, J.D. Prades, et al., Printed sensor labels for colorimetric detection of ammonia, formaldehyde and hydrogen sulfide from the ambient air, Sens. Actuators B Chem. 330 (2021) 129281.
[39] R.E. Owyeung, M.J. Panzer, S.R. Sonkusale, Colorimetric gas sensing washable threads for smart textiles, Sci. Rep. 9 (2019) 5607.
[40] J. Shin, G.S. Kim, S. Ha, T. Yoon, J. Lee, T. Lee, et al., Artificially intelligent nasal perception for rapid sepsis diagnostics, NPJ Digit. Med. 8 (2025) 476.
[41] H.S. Wasisto, J.D. Prades, J. Gülink, A. Waag, Beyond solid-state lighting: Miniaturization, hybrid integration, and applications of gan nano- and micro-leds, Appl. Phys. Rev. 6 (2019) 041315.
[42] W.Z. Wu, F.N. Stapelfeldt, S. Kroker, H.S. Wasisto, A. Waag, A compact calibratable pulse oximeter based on color filters: Towards a quantitative analysis of measurement uncertainty, IEEE Sens. J. 21 (2021) 7522–7531.
[43] S. Mariana, J. Guelink, G. Hamdana, F. Yu, K. Strempel, H. Spende, et al., Vertical gan nanowires and nanoscale light-emitting-diode arrays for lighting and sensing applications, ACS Appl. Nano Mater. 2 (2019) 4133–4142.
[44] N. Yulianto, A.D. Refino, A. Syring, N. Majid, S. Mariana, P. Schnell, et al., Wafer-scale transfer route for top-down iii-nitride nanowire led arrays based on the femtosecond laser lift-off technique, Microsyst. Nanoeng. 7 (2021) 32.
[45] N. Yulianto, G.T.M. Kadja, S. Bornemann, S. Gahlawat, N. Majid, K. Triyana, et al., Ultrashort pulse laser lift-off processing of ingan/gan light-emitting diode chips, ACS Appl. Electron. Mater. 3 (2021) 778–788.
[46vE.A. Prasetyanto, H.S. Wasisto, D. Septiadi, Cellular lasers for cell imaging and biosensing, Acta Biomater. 143 (2022) 39–51.
[47] P. Yajan, N. Yulianto, M. Saba, A.B. Dharmawan, M.S. de Almeida, P. Taladriz-Blanco, et al., Intracellular gold nanoparticles influence light scattering and facilitate amplified spontaneous emission generation, J. Colloid Interface Sci. 622 (2022) 914–923.
[48] A. Kononov, B. Korotetsky, I. Jahatspanian, A. Gubal, A. Vasiliev, A. Arsenjev, et al., Online breath analysis using metal oxide semiconductor sensors (electronic nose) for diagnosis of lung cancer, J. Breath Res. 14 (2020) 016004.
[49] J. Han, H. Li, J. Cheng, X. Ma, Y. Fu, Advances in metal oxide semiconductor gas sensor arrays based on machine learning algorithms, J Mater. Chem. C. 13 (2025) 4285–4303.
[50] Y.G. Song, Y.S. Shim, J.M. Suh, M.S. Noh, G.S. Kim, K.S. Choi, et al., Ionic-activated chemiresistive gas sensors for room-temperature operation, Small 15 (2019) 1902065.
[51] M. Verma, G. Bahuguna, A. Saharan, S. Gaur, H. Haick, R. Gupta, Room temperature humidity tolerant xylene sensor using a sn-sno2 nanocomposite, ACS Appl. Mater. Interfaces 15 (2023) 5512–5520.
[52] G.S. Kim, H. Kum, J.W. An, H. Kwon, Y.J. Ryu, H.W. Jang, et al., Ultrafast photothermal-shock-driven multimetallic exsolution for artificial olfaction of sulfur compounds detection, Small Struct. 6 (2025) 2500292.
[53] D.Z. Zhang, Q. Mi, D.Y. Wang, T.T. Li, Mxene/co_3o_4 composite based formaldehyde sensor driven by zno/mxene nanowire arrays piezoelectric nanogenerator, Sens. Actuators B Chem. 339 (2021) 129923.
[54] R. Paul, B. Das, R. Ghosh, Novel approaches towards design of metal oxide based hetero-structures for room temperature gas sensor and its sensing mechanism: A recent progress, J. Alloys Compd. 941 (2023) 168943.
[55] D. Wong, O. Abuzalat, S. Mostafa, S.S. Park, S. Kim, Intense pulsed light-based synthesis of hybrid tio2-sno2/mwcnt doped cu-btc for room temperature ammonia sensing, J Mater. Chem. C 8 (2020) 7567–7574.
[56] Y.L. Wang, J. Liu, X.B. Cui, Y. Gao, J. Ma, Y. Sun, et al., Nh3 gas sensing performance enhanced by pt-loaded on mesoporous WO3, Sens. Actuators B Chem. 238 (2017) 473–481.
[57] N. Zhang, X.Y. Li, H.C. Ye, S.M. Chen, H.X. Ju, D. Liu, et al., Oxide defect engineering enables to couple solar energy into oxygen activation, J. Am. Chem. Soc. 138 (2016) 8928–8935.
[58] X. Wang, T.K. Wang, G.K. Si, Y. Li, S.W. Zhang, X.L. Deng, et al., Oxygen vacancy defects engineering on ce-doped α-fe2o3 gas sensor for reducing gases, Sens. Actuators B Chem. 302 (2020) 127165.
[59] B.X. Yang, J.Y. Liu, H. Qin, Q. Liu, X.Y. Jing, H.Q. Zhang, et al., Pto2-nanoparticles functionalized cuo polyhedrons for n-butanol gas sensor application, Ceram. Int. 44 (2018) 10426–10432.
[60] L.B. Cai, X.Q. Dong, G.G. Wu, J.P. Sun, N. Chen, H.Z. Wei, et al., Ultrasensitive acetone gas sensor can distinguish the diabetic state of people and its high performance analysis by first-principles calculation, Sens. Actuators B Chem. 351 (2022) 130863.
[61] G. Ciprandi, A. Signori, M. A. Tosca, I. Cirillo, Bronchodilation test in patients with allergic rhinitis, Allergy 66 (2011) 694–698.
[62] G.S. Kim, Y. Lim, J. Shin, J. Yim, S. Hur, H.C. Song, et al., Breathable mofs layer on atomically grown 2d sns2 for stable and selective surface activation, Adv. Sci. 10 (2023) 2301002.
[63] Z. Liu, X. Yang, J. Sun, F. Ma, PVDF modified pd-sno2 hydrogen sensor with stable response under high humidity, Mater. Lett. 212 (2018) 283–286.

[64] Z. Gao, G. Song, X. Zhang, Q. Li, S. Yang, T. Wang, et al., A facile pdms coating approach to room-temperature gas sensors with high humidity resistance and long-term stability, Sens. Actuators B Chem. 325 (2020) 128810.
[65] H.R. Kim, A. Haensch, I.D. Kim, N. Barsan, U. Weimar, J.H. Lee, The role of nio doping in reducing the impact of humidity on the performance of sno2-based gas sensors: Synthesis strategies, and phenomenological and spectroscopic studies, Adv. Funct. Mater. 21 (2011) 4456–4463.
[66] J.W. Yoon, J.S. Kim, T.H. Kim, Y.J. Hong, Y.C. Kang, J.H. Lee, A new strategy for humidity independent oxide chemiresistors: Dynamic self-refreshing of in2o3 sensing surface assisted by layer-by-layer coated ceo2 nanoclusters, Small 12 (2016) 4229–4240.
[67] Y. Sun, Z. Zhao, K. Suematsu, P. Li, Z. Yu, W. Zhang, et al., Rapid and stable detection of carbon monoxide in changing humidity atmospheres using clustered in2o3/cuo nanospheres, ACS Sens. 5 (2020) 1040–1049.
[68] H. Wang, M. Chen, Q. Rong, Y. Zhang, J. Hu, D. Zhang, et al., Ultrasensitive xylene gas sensor based on flower-like sno2/co3o4 nanorods composites prepared by facile two-step synthesis method, Nanotechnology 31 (2020) 255501.
[69] L. Morawska, G.R. Johnson, Z.D. Ristovski, M. Hargreaves, K. Mengersen, S. Corbett, et al., Size distribution and sites of origin of droplets expelled from the human respiratory tract during expiratory activities, J. Aerosol Sci. 40 (2009) 256–269.
[70] A. Ari, Practical strategies for a safe and effective delivery of aerosolized medications to patients with covid-19, Respir. Med. 167 (2020) 105987.
[71] Y.H. Cho, D.S. Kim, J.H. Seo, J.H. Chung, Z. Park, K.C. Kwon, et al., Artificial olfactory system enabled by ultralow chemical sensing variations of 1d sno2 nanoarchitectures, Adv. Sci. 12 (2025) 2501293.
[72] W. Ku, G. Lee, J.-Y. Lee, D.-H. Kim, K.-H. Park, J. Lim, et al., Rational design of hybrid sensor arrays combined synergistically with machine learning for rapid response to a hazardous gas leak environment in chemical plants, J. Hazard. Mater. 466 (2024) 133649.
[73] B. Zong, S. Wu, Y. Yang, Q. Li, T. Tao, S. Mao, Smart gas sensors: Recent developments and future prospective, Nano-Micro Lett. 17 (2025) 54.
[74] W.Q. Cao, Y.X. Duan, Current status of methods and techniques for breath analysis, Crit. Rev. Anal. Chem. 37 (2007) 3–13.
[75] A. Amann, P. Spanel, D. Smith, Breath analysis: The approach towards clinical applications, Mini Rev. Med. Chem. 7 (2007) 115–129.
[76] D. Smith, T.S. Wang, J. Sulé-Suso, P. Spanel, A. El Haj, Quantification of acetaldehyde released by lung cancer cells in vitro using selected ion flow tube mass spectrometry, Rapid Commun. Mass Spectrom. 17 (2003) 845–850.
[77] P.C. Kamat, C.B. Roller, K. Namjou, J.D. Jeffers, A. Faramarzalian, R. Salas, et al., Measurement of acetaldehyde in exhaled breath using a laser absorption spectrometer, Appl. Opt. 46 (2007) 3969–3975.
[78] G. Giubileo, Medical diagnostics by laser-based analysis of exhaled breath, Proceedings of the International Conference on Advanced Laser Technologies (ALT'01), Constanţa, Romania, 2002, pp. 318–325.
[79] C. Di Natale, A. Macagnano, E. Martinelli, R. Paolesse, G. D'Arcangelo, C. Roscioni, et al., Lung cancer identification by the analysis of breath by means of an array of non-selective gas sensors, Biosens. Bioelectron. 18 (2003) 1209–1218.
[80] F. Röck, N. Barsan, U. Weimar, Electronic nose: Current status and future trends, Chem. Rev. 108 (2008) 705–725.
[81] A.D. Wilson, Application of electronic-nose technologies and voc-biomarkers for the noninvasive early diagnosis of gastrointestinal diseases, Sensors 18 (2018) 2613.
[82] A. Jemal, R. Siegel, E. Ward, Y.P. Hao, J.Q. Xu, T. Murray, et al., Cancer statistics, 2008, CA Cancer J. Clin. 58 (2008) 71–96.
[83] D. Smith, P. Španěl, A.A. Fryer, F. Hanna, G.A. Ferns, Can volatile compounds in exhaled breath be used to monitor control in diabetes mellitus?, J. Breath Res. 5 (2011) 022001.
[84] W. Ping, T. Yi, H.B. Xie, F.R. Shen, A novel method for diabetes diagnosis based on electronic nose, Biosens. Bioelectron. 12 (1997) 1031–1036.
[85] N. Makisimovich, V. Vorotyntsev, N. Nikitina, O. Kaskevich, P. Karabun, F. Martynenko, Adsorption semiconductor sensor for diabetic ketoacidosis diagnosis, Sens. Actuators B Chem. 36 (1996) 419–421.
[86] B. Solnica, J.W. Naskalski, J. Sieradzki, Analytical performance of glucometers used for routine glucose self-monitoring of diabetic patients, Clin. Chim. Acta. 331 (2003) 29–35.
[87] M. Gerard, A. Chaubey, B.D. Malhotra, Application of conducting polymers to biosensors, Biosens. Bioelectron. 17 (2002) 345–359.
[88] M. Fleischer, E. Simon, E. Rumpel, H. Ulmer, M. Harbeck, M. Wandel, et al., Detection of volatile compounds correlated to human diseases through breath analysis with chemical sensors, Sens. Actuators B Chem. 83 (2002) 245–249.
[89] D. Poli, P. Carbognani, M. Corradi, M. Goldoni, O. Acampa, B. Balbi, et al., Exhaled volatile organic compounds in patients with non-small cell lung cancer: Cross sectional and nested short-term follow-up study, Respir. Res. 6 (2005) 71.
[90] Y. Suzuki, J. Saito, M. Munakata, Y. Shibata, Hydrogen sulfide as a novel biomarker of asthma and chronic obstructive pulmonary disease, Allergol. Int. 70 (2021) 181–189.
[91] H. Shin, D.H. Kim, W. Jung, J.S. Jang, Y.H. Kim, Y. Lee, et al., Surface activity-tuned metal oxide chemiresistor: Toward direct and quantitative halitosis diagnosis, Acs Nano 15 (2021) 14207–14217.
[92] D.L. Feng, L.L. Du, X.X. Xing, C. Wang, J. Chen, Z.Y. Zhu, et al., Highly sensitive and selective nio/wo3 composite nanoparticles in detecting h2s biomarker of halitosis, ACS Sens. 6 (2021) 733–741.
[93]]]]N.H. Kim, S.J. Choi, D.J. Yang, J. Bae, J. Park, I.D. Kim, Highly sensitive and selective hydrogen sulfide and toluene

sensors using pd functionalized wo3 nanofibers for potential diagnosis of halitosis and lung cancer, Sens. Actuators B Chem. 193 (2014) 574–581.
[94] X.W. Jing Zhang, Y. Chen, W. Yao, Correlation between levels of exhaled hydrogen sulfide and airway inflammatory phenotype in patients with chronic persistent asthma, Respirology 19 (2014) 1165–1169.
[95] J. Cui, F. Li, Z. L. Shi, Origin and evolution of pathogenic coronaviruses, Nat. Rev. Microbiol. 17 (2019) 181–192.
[96] B. Hu, H. Guo, P. Zhou, Z.L. Shi, Characteristics of sars-cov-2 and covid-19, Nat. Rev. Microbiol. 19 (2021) 141–154.
[97] F. Krammer, Sars-cov-2 vaccines in development, Nature 586 (2020) 516–527.
[98] J. Yang, X.H. Chen, X.W. Deng, Z.Y. Chen, H. Gong, H. Yan, et al., Disease burden and clinical severity of the first pandemic wave of covid-19 in wuhan, china, Nat. Commun. 11 (2020) 5411.
[99] J.P. Mathuria, R. Yadav, Rajkumar, Laboratory diagnosis of sars-cov-2-a review of current methods, J. Infect. Public Health 13 (2020) 901–905.
[100] Y.W. Tang, J.E. Schmitz, D.H. Persing, C.W. Stratton, Laboratory diagnosis of covid-19: Current issues and challenges, J. Clin. Microbiol. 58 (2020) e00512–20.
[101] T. X. Ji, Z.W. Liu, G.Q. Wang, X.G. Guo, S.A. Khan, C.C. Lai, H.Y. Chen, et al., Detection of covid-19: A review of the current literature and future perspectives, Biosens. Bioelectron. 166 (2020) 112455.
[102] S.A. Harmon, T.H. Sanford, S. Xu, E.B. Turkbey, H. Roth, Z.Y. Xu, et al., Artificial intelligence for the detection of covid-19 pneumonia on chest ct using multinational datasets, Nat. Commun. 11 (2020) 4080.
[103] F. Khatami, M. Saatchi, S.S.T. Zadeh, Z.S. Aghamir, A.N. Shabestari, L.O. Reis, et al., A meta-analysis of accuracy and sensitivity of chest ct and rt-pcr in covid-19 diagnosis, Sci. Rep. 10 (2020) 22402.
[104] M. Park, J. Won, B.Y. Choi, C.J. Lee, Optimization of primer sets and detection protocols for sars-cov-2 of coronavirus disease 2019 (covid-19) using pcr and real-time pcr, Exp. Mol. Med. 52 (2020) 963–977.
[105] P. Pokhrel, C.P. Hu, H.B. Mao, Detecting the coronavirus (covid-19), ACS Sens. 5 (2020) 2283–2296.
[106] R.A.S. Martínez, J.M.P. Hernández, O.Y. Torrado, M.C. Díaz, T.D. Puente, M.V. Crevillent, Exhaled volatile organic compounds analysis in clinical pediatrics: A systematic review, Pediatr. Res. 89 (2021) 1352–1363.
[107] S.M. Fernando, A. Tran, W. Cheng, M. Klompas, K. Kyeremanteng, S. Mehta, et al., Diagnosis of ventilator-associated pneumonia in critically ill adult patients-a systematic review and meta-analysis, Intensive Care Med. 46 (2020) 1170–1179.
[108] C. Sanchez, J.P. Santos, J. Lozano, Use of electronic noses for diagnosis of digestive and respiratory diseases through the breath, Biosensors 9 (2019) 35.
[109] A.M.I. Saktiawati, Y. Stienstra, Y.W. Subronto, N. Rintiswati, Sumardi, J.W. Gerritsen, et al., Sensitivity and specificity of an electronic nose in diagnosing pulmonary tuberculosis among patients with suspected tuberculosis, PLoS One 14 (2019) e0217963.
[110] A.G.W.E. Wintjens, K.F.H. Hintzen, S.M.E. Engelen, T. Lubbers, P.H.M. Savelkoul, G. Wesseling, et al., Applying the electronic nose for pre-operative sars-cov-2 screening, Surg. Endosc. 35 (2021) 6671–6678.
[111] T.C. Miller, S.D. Morgera, S.E. Saddow, A. Takshi, M. Mullarkey, M. Palm, Neurological connections and endogenous biochemistry - potentially useful in electronic-nose diagnostics for coronavirus diseases, Neurol. Neuroimmunol. Neuroinflamm. 8 (2021) 284.
[112] O. Lawal, W.M. Ahmed, T.M.E. Nijsen, R. Goodacre, S.J. Fowler, Exhaled breath analysis: A review of 'breath-taking' methods for off-line analysis, Metabolomics 13 (2017) 110.
[113] A. Tiele, A. Wicaksono, E. Daulton, E. Ifeachor, V. Eyre, S. Clarke, et al., Breath-based non-invasive diagnosis of alzheimer's disease: A pilot study, J. Breath Res. 14 (2020) 026003.
[114] S. Bevc, E. Mohorko, M. Kolar, P. Brglez, A. Holobar, D. Kniepeiss, et al., Measurement of breath ammonia for detection of patients with chronic kidney disease, Clin. Nephrol. 88 (2017) S14–S17.
[115] V. Saasa, M. Beukes, Y. Lemmer, B. Mwakikunga, Blood ketone bodies and breath acetone analysis and their correlations in type 2 diabetes mellitus, Diagnostics 9 (2019) 224.
[116] L. Zhang, S. Liu, M. Li, X.F. Xu, Diagnostic value of fractional exhaled nitric oxide in cough-variant asthma: An updated meta-analysis, J. Asthma 57 (2020) 335–342.
[117] J.C. He, B.H. Pu, H.J. Ding, H. Wang, Method for predicting clinical state of disease based on information technology on diagnosis in chinese medicine, Proceedings of the 2008 IEEE International Symposium on IT in Medicine and Education, Xiamen, China, 2008, pp. 583–586.
[118] S. Haze, Y. Gozu, S. Nakamura, Y. Kohno, K. Sawano, H. Ohta, et al., 2-nonenal newly found in human body odor tends to increase with aging, J. Invest. Dermatol. 116 (2001) 520–524.
[119] A. Agapiou, E. Zorba, K. Mikedi, L. McGregor, C. Spiliopoulou, M. Statheropoulos, Analysis of volatile organic compounds released from the decay of surrogate human models simulating victims of collapsed buildings by thermal desorption-comprehensive two-dimensional gas chromatography-time of flight mass spectrometry, Anal. Chim. Acta. 883 (2015) 99–108.
[120] A. Lalvani, M. Pareek, A 100 year update on diagnosis of tuberculosis infection, Br. Med. Bull. 93 (2010) 69–84.
[121] D.G. Russell, Mycobacterium tuberculosis: Here today, and here tomorrow, Nat. Rev. Mol. Cell Biol. 2 (2001) 569–578.
[122] S.G. de Vries, A.L. Cremers, C.C. Heuvelings, P.F. Greve, B.J. Visser, S. Bélard, et al., Barriers and facilitators to the uptake of tuberculosis diagnostic and treatment services by hard-to-reach populations in countries of low and medium tuberculosis incidence: A systematic review of qualitative literature, Lancet Infect. Dis. 17 (2017) E128–E143.
[123] C.L. Lu, Q. Liu, A. Sarma, C. Fitzpatrick, D. Falzon, C.D. Mitnick, A systematic review of reported cost for smear

and culture tests during multidrug-resistant tuberculosis treatment, PLoS One 8 (2013) e56074.
[124] K. Siddiqi, M.L. Lambert, J. Walley, Clinical diagnosis of smear-negative pulmonary tuberculosis in low-income countries: The current evidence, Lancet Infect. Dis. 3 (2003) 288–296.
[125] K.R. Steingart, H. Sohn, I. Schiller, L.A. Kloda, C.C. Boehme, M. Pai, et al., Xpert® mtb/rif assay for pulmonary tuberculosis and rifampicin resistance in adults (review), Cochrane Database Syst. Rev. (2013) CD009593.
[126] I. Pathmanathan, A. Date, W.L. Coggin, J. Nkengasong, A.S. Piatek, H. Alexander, Rolling out xpert mtb/rif® for tuberculosis detection in hiv-positive populations: An opportunity for systems strengthening, Afr. J. Lab. Med. 6 (2017) 1–9.
[127] World Health Organization (WHO), High priority target product profiles for new tuberculosis diagnostics: Report of a consensus meeting, World Health Organization, Geneva, Switzerland, 2014.
[128] D.A. Ahlburg, The economic impacts of tuberculosis, World Health Organization, Geneva, Switzerland, 2000.
[129] S. Riazanskaia, G. Blackburn, M. Harker, D. Taylor, C.L.P. Thomas, The analytical utility of thermally desorbed polydimethylsilicone membranes for - sampling of volatile organic compounds in and on human skin, Analyst 133 (2008) 1020–1027.
[130] J. Rane, R.A. Chaudhari, N.L. Rane, Enhancing supply chain resilience through generative artificial intelligence, explainable AI, and federated learning, in: J. Rane, R.A. Chaudhari, N.L. Rane (Eds.), Enhancing sustainable supply chain resilience through artificial intelligence and machine learning: Industry 4.0 and industry 5.0 in manufacturing, Deep Science Publishing, London, 2025, p. 163.
[131] L. Albshaier, S. Almarri, A. Albuali, Federated learning for cloud and edge security: A systematic review of challenges and ai opportunities, Electronics 14 (2025) 1019.
[132] M. Aledhari, R. Razzak, R.M. Parizi, F. Saeed, Federated learning: A survey on enabling technologies, protocols, and applications, IEEE Access 8 (2020) 140699–140725.
[133] Q. Yang, Toward responsible ai: An overview of federated learning for user-centered privacy-preserving computing, ACM Trans. Interact. Intell. Syst. 11 (2021) 1–22.

Jung-Won An received his B.S. degree in School of Materials Science and Engineering from Pusan National University in 2022. Since then, he is now a Ph.D. candidate under the co-guidance of Dr. Ji-Soo Jang in Korea Institute of Science and Technology (KIST) and Prof. Ho Won Jang in Seoul National University. His current research includes material synthesis and device fabrication for chemical sensors, and micro-LEDs

Ji-Soo Jang is a senior research scientist in the Electronic Materials Research Center at the Korea Institute of Science and Technology (KIST). He received his Ph.D. degree from the Department of Materials Science and Engineering at KAIST in 2020. After earning his Ph.D., he moved to Yale University as a postdoctoral associate from 2020 to 2021. His current research interests include the design of various functional materials, chemical sensors, environmental materials, energy harvesting, and water treatment. For more information, please visit the website: https://wkdwltn92.wixsite.com/starlab